Published in : Chemical Physics (2009), vol 365, iss. 3, pp109-128
Status: Postprint (Author's version)

Medium and high resolution vacuum UV photoabsorption spectroscopy of methyl iodide (CH_3I) and its deuterated isotopomers CD_3I and CH_2DI. A Rydberg series analysis

R. Locht[a], B. Leyh[a], H.W. Jochims [b], H. Baumgartel[b]

[a]*Laboratoire de Dynamique Moléculaire, Département de Chimie, Institut de Chimie, Bât.B6c, Université de Liège, Sart-Tilman par, B-4000 Liège* 1, *Belgium*
[b]*Institut für Physikalische und Theoretische Chemie, Freie Universität Berlin, Takustraße 3,* D-14195 *Berlin, Germany*

Abstract

The vacuum UV photoabsorption spectrum of CH_3I has been investigated between 5 eV and 20 eV. Numerous vibronic transitions are observed. In the high 10-20 eV photon energy range weak to very weak diffuse bands are observed and ascribed to electronic transitions from $3a_1$, 1e and $2a_1$ to Rydberg orbitals. In the 6-10.5 eV photon energy range more than 200 sharp and strong to weak lines have been observed. Several photon energy ranges were explored under high resolution conditions allowing us to observe many series up to high values of the principal quantum number *n*. They are assigned to vibration-less Rydberg transitions and classified into two groups converging to the two components of the spin-orbit split $\tilde{X}\,^2E$ state of CH_3I^+. These two groups consist of six different Rydberg series, i.e., *n*sa_1, *n*pa_1, *n*pe, *n*da_1, *n*de and *n*f. A very close correlation has been established between the term values of the Rydberg states in CH_3I and in Xe for *n*s, *n*p, *n*d and *n*f Rydberg transitions. For the first time, the same measurements have been performed and the interpretation has been proposed for the photoabsorption spectrum of CH_2DI and CD_3I in the 6-10.5 eV photon energy range. For these two species, ionization energies are deduced: for the $\tilde{X}\,^2E_{3/2}$ and $\tilde{X}\,^2E_{1/2}$ states of CH_2DI, these are IE_{ad} = 9.544 eV and IE_{ad} = 10.168 eV, respectively, and the corresponding energies are 9.552 eV and 10.173 eV in CD_3I.

Keywords: V-UV photoabsorption**;** Medium and high resolution; Synchrotron radiation; Rydberg states; Ab initio calculations; Ionization energies; Isotopomers; CH_3I; CD_3I; CH_2DI

1. INTRODUCTION

Iodine is a minor constituent in the Earth's atmosphere but its ozone depleting efficiency is estimated to be about 300 to 1000-fold larger than that of chlorine [1]. Its major sources are volatile organic iodides, mainly CH_3I. The highest concentrations are observed at the marine boundary layer and mostly assigned to biogenic processes [1,2]. Anthropogenic contributions are negligible [2]. Iodine atoms are released essentially by photolysis initiating various reactions in both the troposphere and the stratosphere [1,2]. It has been suggested [2] that the coupling of a low natural abundance of iodine with increasing bromine and chlorine levels has contributed to the trend towards ozone loss in the higher troposphere and lower stratosphere [1].

The permanent nature of methyl iodide as a polluting agent and the associated production mechanisms of iodine are strong incentives for the investigation of its photophysics.

Several photoabsorption studies of CH3I have been reported in the literature. The first vacuum UV photoabsorption spectrum of CH_3I was photographed by Price [3] in the wavelength region of 201-121.5 nm (6.17-10.20 eV) using a grazing incidence spectrograph and the Lymann continuum as an excitation source. In the 140-121.5 nm region this author classified the observed bands into six Rydberg series with quantum defects of 0.75, 0.50, 1.0, 0.75, 0.55 and 0.95, respectively. These converge to the two first ionization limits identified at 76 930 cm^{-1} and 81 990 cm^{-1}.

The first absolute photoabsorption spectrum of CH3I was reported by Boschi and Salahub [4] who recorded the spectra of several iodoalkanes between 30 000 cm^{-1} and 90 000 cm^{-1} with a 1 m normal incidence (NIM) spectrophotometer with a double beam setup. A rough analysis of the Rydberg series is presented and a correlation between the term values measured in CH_3I and Xe is established for the first time. The emphasis is also put on the comparison between the vibrational structure in the first members of the ns Rydberg series and in the first band of the photoelectron spectrum of CH_3I.

Hochmann et al. [5] and Felps et al. [6] studied the Rydberg transitions in the methyl halides CH_3Cl, CH_3Br and CH_3I. In the former work, the authors analyzed the spectra on the basis of a linear correlation between the energy of the Rydberg transitions and the ionization energies. In the latter publication the authors restricted their study to the lowest s-type Rydberg transition in both the hydrogenated and perdeuterated methyl halides and presented vibrational assignments. In a later work Felps et al. [7] reported the electronic spectra of the methyl and cyanogen halides without any detailed analysis of the methyl halides.

Wang et al. [8] reexamined the V-UV spectra of CH_3I and HI. The Rydberg series in these molecular systems are shown to exhibit quantum defect analogies to the corresponding series in Xe. This method is applied to the ns and nd series converging to both the ionization limits $^2E_{3/2}$ and $^2E_{1/2}$ of CH_3I^+.

Baig et al. [9] and Dagata et al. [10] were the first to report on high resolution V-UV photoabsorption spectroscopy of CH_3I using a 3 m-NIM spectrograph equipped with a 5000 l/mm Al-MgF_2 grating. Synchrotron radiation is used as excitation source. The 0, N, and C emissions obtained by a hollow cathode discharge in air are used for calibration. Strong quantum defect analogies between Xe and CH_3I are demonstrated even for high quantum numbers. These were confirmed by a multichannel quantum defect (MQDT) theoretic analysis of the data. A new d-series converging to the first ionization limit is assigned.

Most recently, Eden et al. [11] investigated the V-UV spectra of CH_3I and CH_3Cl using synchrotron radiation. These authors measured the photoabsorption cross section between 3 eV and 10.8 eV photon energy. A Rydberg series and a vibrational structure analysis are reported.

For the purpose of environmental chemical investigations, Fahr et al. [12] published results on the temperature dependence of the V-UV absorption spectrum cross section of CH_3I in both the gas and the liquid phase. With increasing temperature the high energy (120-210 nm) photoabsorption cross section increases whereas the 210-270 nm absorption cross section decreases.

The most recent good resolved (0.05 eV FWHM) electron energy loss spectroscopic (e, e) measurements on CH_3I were reported by Olney et al. [13] between 4eV and 25 eV They also derived the oscillator strength (related to the cross section and the extinction coefficient) for absorption of CH_3I between 4.5 eV and 488 eV at low resolution (1 eV FWHM).

During the last decade our laboratory paid a lot of attention to the V-UV spectroscopy, the photoelectron spectroscopy [Threshold (TPES), Constant Ion State (CIS) and He-I] and the mass spectro-metric photoionization of the monohalogenated derivatives of methane, i.e., CH_3F [14-17], CH_3C1 [18-20], and recently CH_3Br [21-23].

In the present contribution we report on the medium and high resolution photoabsorption spectrum of CH_3I measured in the 6-25 eV photon energy range using synchrotron radiation. To the best of our knowledge, the photoabsorption spectra of CD_3I and CH_2DI as observed between 6 eV and 12 eV photon energy is reported for the first time. The present paper focuses on the detailed investigation of the vibrationless Rydberg transitions in CH_3I, CD_3I and CH_2DI. The vibrational structure will be examined in a forthcoming publication [24].

2. EXPERIMENTAL

2.1. Experimental setup

The experimental setup used in this work has already been described in detail elsewhere [25]. Only the most salient features will be reported here. Furthermore, two monochromators, as recently commissioned at the BESSY II synchrotron radiation facility, have been used.

In a first series of experiments, synchrotron radiation available from the BESSY I facility (Berlin, Germany) was dispersed with a modified vacuum UV normal incidence 225 McPherson monochro-mator with a focal length of 1.5 m, instead of 1 m in the commercial version (1 m-NIM-2 beamline). A laminar Zeiss grating is used for the efficient reduction of the 2nd spectral order. It is gold-coated with 1200 ℓ/mm and its transmission breaks down above 26 eV (210 000 cm^{-1} or 47 nm). The width of the entrance and exit slits of 100 µm ensures a 0.1 nm wavelength resolution corresponding to a resolving power of about 1200 at 10 eV. This monochromator is used for the recording of absolute photoabsorption spectra in the 5-25 eV and 5-11.5 eV photon energy ranges.

The 3 m-NIM-2 beamline at the BESSY II facility (Berlin, Germany) has been described by Reichardt et al. [26]. This 3 m-NIM monochromator is positioned at a bending magnet front end. It is equipped with two spherical gratings, i.e., an Al/MgF_2-grating of 600 ℓ/mm and a Pt-grating of 2400 ℓ/mm allowing us to cover the 5-55 eV photon energy range. The latter grating has its optimal transmission between l0 eV and 40 eV (124-31 nm). The entrance and exit slits were adjusted between 25 and 40 µm leading to a resolving power of 25 000-13 000 at 10 eV (124 nm) photon energy. This monochromator was used for recording high resolution spectra, covering 50-500 meV photon energy ranges. Most of the spectra discussed in the present work were measured with 30 µm entrance and exit slits and using the 2400 ℓ/mm Pt-grating.

Recently, a 10 m-NIM monochromator has been started up at BESSY II [27]. It is positioned at the UE-125 undulator front end. Combined movement of the monochromator and the undulator gap is required for scanning the wavelength of the light source. This monochromator is equipped with two gratings: a gold-coated 300 1/mm grating and a 1200ℓ/mm Pt-grating. The entrance (S_1) and exit (S_2) slits were adjusted between 5 µm and 25 µm. In optimal operating conditions a resolving power of 125 000 is expected and 114 000 is obtained at $h\nu \approx 20$eV [27], the monochromator being optimized for photon energies $h\nu \geq 15$ eV. However, at lower energy, i.e., $h\nu \leq 10$ eV, the transmitted intensity becomes low. The effective resolution power also drops and is estimated to be in the order of 40 000 in the present operating conditions, i.e., at $h\nu \leq 10$ eV and with $S_1 = 20$ µm and $S_2 = 5$ µm using the 1200ℓ/ mm Pt-grating. For photon energies $h\nu \approx 6$ eV the signal/noise ratio becomes very low and the undulator gap is at its upper limit. This feature prevents us from measuring in the 6-8 eV photon energy range.

In all above described setups, at the exit slit of the monochromator the light has to travel through a 1 mm thick stainless steel microchannel plate necessary to maintain a differential pressure of 1:1000 before entering a 30 cm long stainless steel absorption cell. Most spectra are recorded without filter on the light path. However, in some cases a LiF filter (cutoff at 11.8eV or 95 000 cm^{-1} or 105 nm) is used, which can be inserted in the light beam without vacuum breakdown. The vapor pressure in the cell is measured by a Balzers capacitor manometer. The light is detected by a sodium salicylate sensitized photomultiplier located at the end of the absorption cell and in front of the absorption cell entrance slit. Output pulses are recorded by a 100 MHz counter. The recording of an absorption spectrum requires one scan with gas in the absorption cell and one with the empty cell. The stability of the synchrotron radiation and of the pressure in the cell ensured reliable absorption data. If required, the spectra presented in the following sections are corrected for any pressure drift. The sample pressure has been maintained at 15-25µbar to avoid saturation. This was tested by observing the presence of fine structure in the first two strongest absorption bands. The commercially available CH_3I, purchased from Aldrich and of 99.5% purity, was used without further purification. The CD_3I and CH_2DI, purchased from Aldrich are certified at 99.5 and 98 at.% purity, respectively. No noticeable impurity was observed by mass spectrometry at 21.2 eV photon energy. Therefore, the samples were used without further purification.

2.2. Data handling and error estimation

As will be discussed in the next section, in the high photon energy part of the absorption spectrum weak and diffuse structures are superimposed on a strong continuum. To make the identification of these features easier, a continuum subtraction procedure has been applied. This has already been used successfully in previous spectral analysis [17,28]. For this purpose, the experimental curve is severely smoothed to simulate the underlying continuum which is then subtracted from the original photoabsorption spectrum. The smoothing procedure consists in filtering the experimental curve by fast Fourier transform (FFT). The weak features emerge from a remaining strongly attenuated background. The resulting diagram will be called Δ-plot in the forthcoming sections.

The wavelength calibration of the 1.5 m-NIM monochromator has been performed by using the Ar absorption spectrum between the $^2P_{3/2}$ and the $^2P_{1/2}$ ionic states. The accuracy of this calibration is better than 2 meV. In the measurements between 6 eV and 25 eV photon energy, the photoabsorption spectrum has been recorded with an energy interval of about 10 meV. The error on the energy position of a feature is estimated to be 15 meV. In the photoabsorption spectra between 6 eV and 11 eV, an energy increment of 1.5 meV has been adopted. The error on the energy position of a feature is estimated to be of the order of 2 meV. This evaluation is confirmed by the reproducibility of energy positions measured in different spectra recordings over several years. For high resolution spectra recorded with the 3 m-NIM monochromator 50-200 meV photon energy ranges were scanned with 50-200 µeV energy steps. The positioning of the zeroth order wavelength is used for calibration. The accuracy is estimated to be of the order of 1 meV.

Published in : Chemical Physics (2009), vol 365, iss. 3, pp109-128
Status: Postprint (Author's version)

For the 10 m-NIM monochromator the wavelength scale calibration occurred by using the zeroth order positioning. The accuracy is of the order of 0.002 nm [27]. The monochromator has to be scanned on the wavelength scale owing to the combined computer-controlled motion of the grating and of the undulator. For the wavelength-to-energy scale conversion the relation $hc\omega/\lambda$ = 1239.842 eV/nm [29] is used.

In the following sections the comparison between previously published spectra and the data obtained in the present work is presented. However, the numerical data related to the features observed in the literature spectra are often missing. To obtain the numerical energy positions, we scanned and digitized the published spectra by software. This procedure has been applied to the spectra published by Baig and co-workers [10] and Olney et al. [13].

3. EXPERIMENTAL RESULTS

3.1. The CH_3I photoabsorption spectrum

The photoabsorption spectrum of CH_3I has been measured in the 5-25 eV photon energy range. The plot of the molecular extinction coefficient (ε_{hv}) as a function of the photon energy between 5 eV and 20 eV is displayed in Fig. la (with energy steps of 10 meV). The 10-20 eV photon energy range shows a few broad and weak peaks. To characterize these features the subtraction procedure (see Section 2.2) has been applied. The result is shown in Fig. lb.

Fig. 1. *(a) The vacuum UV photoabsorption spectrum of CH_3I in the 5-20 eV photon energy range. The successive ionization continua are indicated, (b) The intensity difference Δ between the photoabsorption spectrum (PAS) and the strongly smoothed photoabsorption spectrum (SMPAS) plotted as a function of the photon energy in the 10-20 eV range. The dashed curve is the result of a FFT smoothing. Assignments of the structures and ionization continua are indicated by vertical bars.*

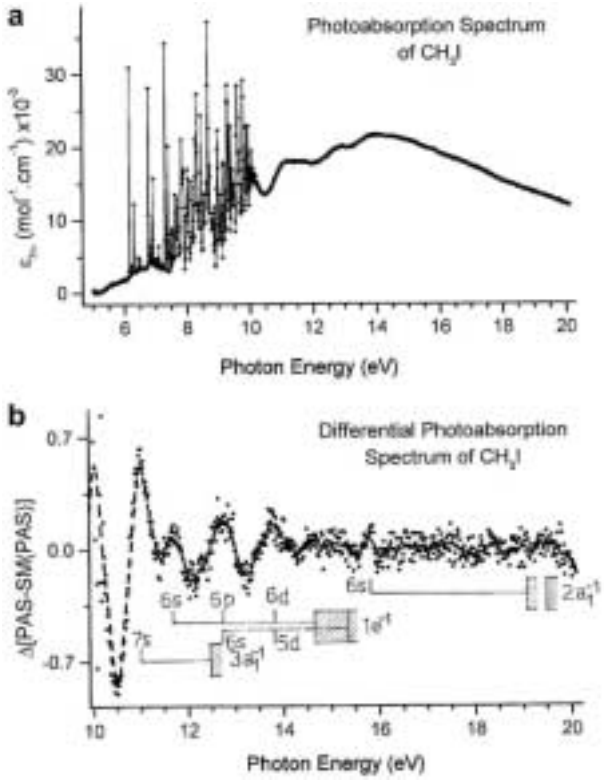

Owing to the data point scattering, a FFT-smoothed curve is drawn through the data points to help the visualization of the structures. The successive ionization energy limits are inserted in this figure. The energy position of the photoabsorption features and the proposed assignments are listed in Table 1 together with the earlier measurements of Olney et al. [13].

Published in : Chemical Physics (2009), vol 365, iss. 3, pp109-128
Status: Postprint (Author's version)

***Table 1**: Position in energy (eV) of Rydberg transitions in the CH_3I photoabsorption spectrum as defined by their band maxima and observed between 10 eV and 20 eV photon energy. Convergence limits data refer to the vertical ionization energy (IE_{vert}) values (eV).*

Band maxima		Convergence limit (eV)	Assignment
This work	[13][a]	[30,34][b]	*n** - Rydberg transitions
11.00	11.1	12.48/12.5 -$3a_1^{-1}$	3.032-$3a_1 \rightarrow$ 7s
11.68	11.8	14.7/14.7 - $1e_{3/2}^{-1}$	2.119 le $\rightarrow$ ($^2E_{3/2}$)6s
12.69	12.7	14.7/14.7-$1e_{3/2}^{-1}$ or 15.4/15.4 -$1e_{1/2}^{-1}$	2.608-le $\rightarrow$ ($^2E_{3/2}$)6p or 3.119-le $\rightarrow$ ($^2E_{1/2}$)6s
13.78	13.6	14.7/14.7-$1e_{3/2}^{-1}$ or 15.4/15.4 - $1e_{1/2}^{-1}$	3.888-le $\rightarrow$ ($^2E_{3/2}$)6d or 2.898-le $\rightarrow$ ($^2E_{1/2}$)5d
15.8	16.4	19.5/19.5/[19.2][b]-$2a_1^{-1}$	2.030-$2a_1 \rightarrow$ 6s
18.4	-		

[a] For explanation, see text: Section 2.2.
[b] For explanation, see discussion Section 4.1.

The rich spectral structure between 5 eV and 11 eV has been explored with the 1.5 m-NIM monochromator using 1.5 meV energy increments. An overview of the photoabsorption spectrum is shown in Fig. 2. Part of the assignments of the main features to Rydberg transitions are inserted in this figure. The convergence limits used in the Rydberg series analysis are ionization energies determined by using Rydberg series analysis [9] and by high resolution He-I photoelectron spectroscopy [30,31].

***Fig. 2.** The vacuum UV photoabsorption spectrum of CH_3I in the 5-11 eV photon energy range recorded with the 1.5 m-NIM. The main vibrationless Rydberg transitions and their respective convergence limit are indicated by vertical bars.*

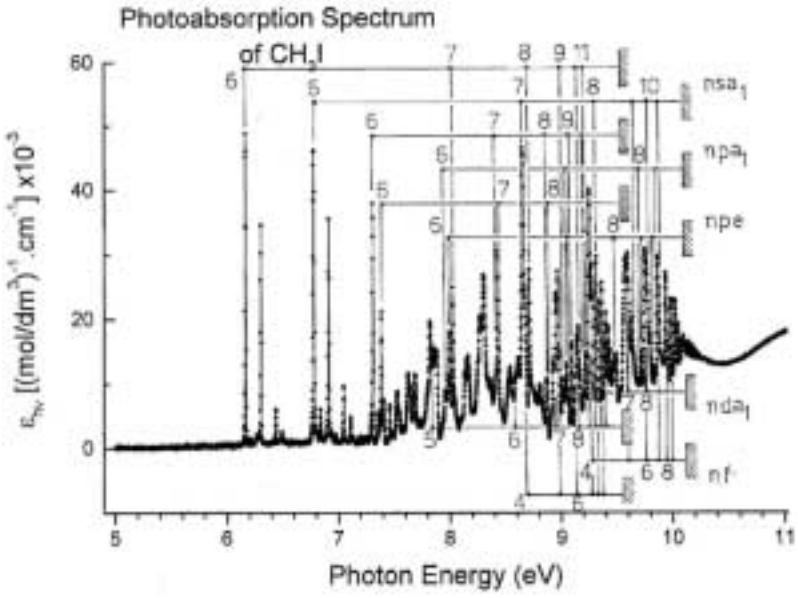

Fig. 3 displays the photoabsorption spectrum of CH_3I on extended energy scales in five different photon energy ranges as measured with the 3 m-NIM or 10 m-NIM monochromator. Assignments of the abundant fine structure are included. The numerical data related to all these features are listed in Table 2 along with the most important previous data [5,9,11] available from the literature.

3.2. The CD_3I photoabsorption spectrum

The absolute photoabsorption spectrum of CD_3I, as observed in the 5-11 eV energy range with the 1.5 m-NIM monochromator is shown in Fig. 4. As long as not too crowded, the assignment of the main features are also included in the figure. The convergence limits drawn in Fig. 4 are the ionization energies determined in an ongoing photoelectron spectroscopic work [31].

Published in : Chemical Physics (2009), vol 365, iss. 3, pp109-128
Status: Postprint (Author's version)

Fig. 3. *The vacuum UV photoabsorption spectrum of CH_3I: (a) in the 8.58-9.03 eV and (b) in the 9.19-9.47 eV ranges with the 3 m-NIM, 2400 ℓ/mm Pt-grating, $S_{entr} = S_{exit} = 50$ µm, p = 32 µbar; (c) in the 9.460-9.525 eV, (d) in the 9.549-9.804 eV and (e) in the 9.970-10.180 eV ranges with the 10 m-NIM, 1200 ℓ/mm Pt-grating $S_{entr} = S_{exit} = 5$ µm. p = 38 µbar. The assignments proposed in this work are included in this figure.*

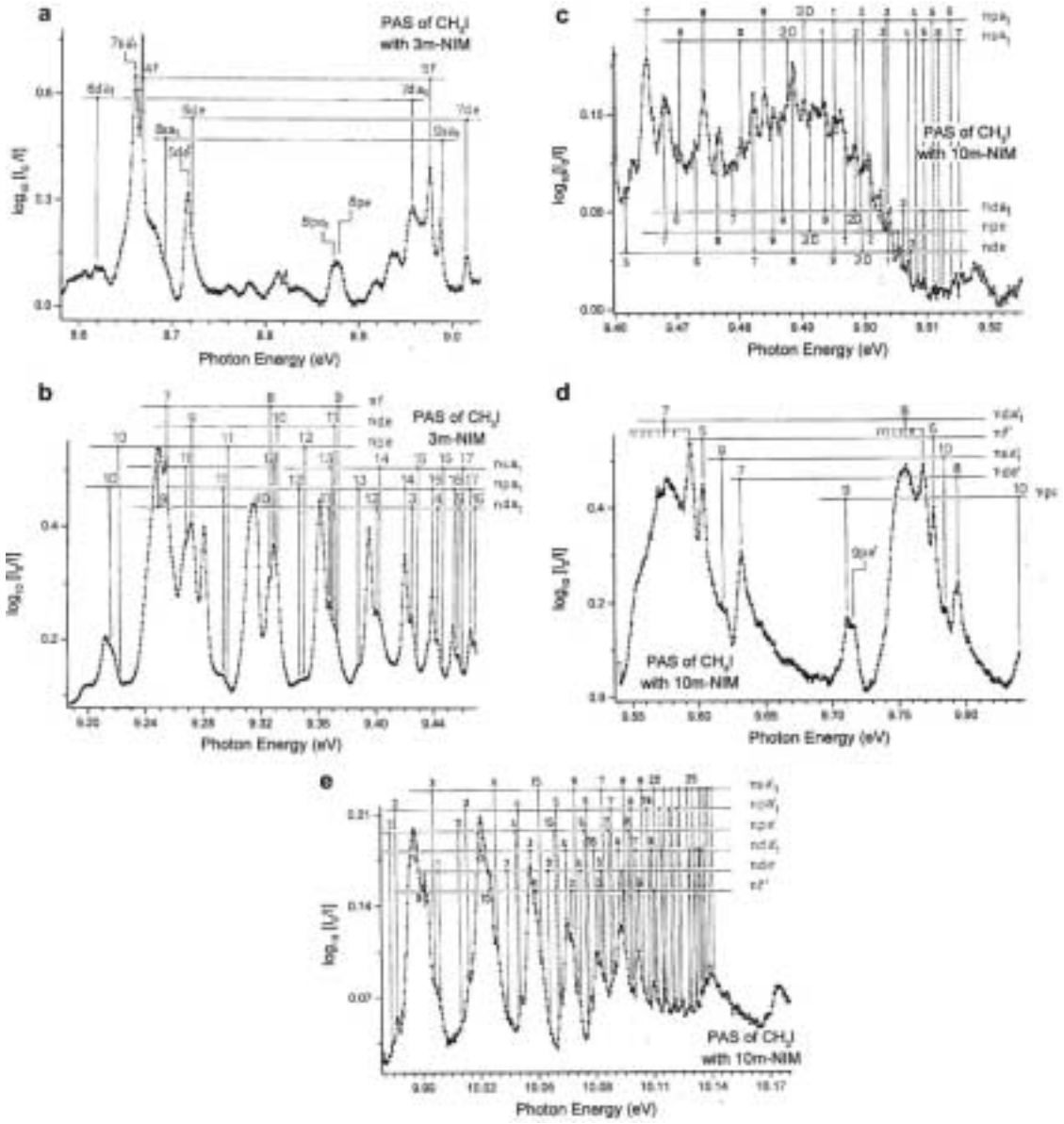

Fig. 5 shows five portions of the photoabsorption spectrum observed at high resolution with the 3 m-NIM or 10 m-NIM monochromator. Assignments of the rich fine structure are included. The numerical data corresponding to these features are listed in Table 3.

3.3. The CH_2DI photoabsorption spectrum

The molecular extinction coefficient ($\varepsilon_{h\nu}$) of CH_2DI as a function of the photon energy between 5.5 eV and 10.5 eV as measured with the 3 m-NIM monochromator (in medium resolution conditions) is drawn in Fig. 6. Assignments of the most intense structures are inserted in this figure. The convergence limits adopted in this work are the ionization energies of CH_2DI measured in a photoelectron spectroscopic work in progress [31].

Published in : Chemical Physics (2009), vol 365, iss. 3, pp109-128
Status: Postprint (Author's version)

***Table 2**: Vibrationless Rydberg transitions as observed for CH_3I in the present work and in previous reports [5,9,11] and converging to both spin-orbit components of the CH_3I^+ (X) state: parts (a) and (b) converge to the $^2E_{3/2}$ and $^2E_{1/2}$ ionic states, respectively. Assignments and effective quantum numbers are included. For the error estimated on the present data, see text (1 eV = 8065.545 cm^{-1} [29]).*

This work			Literature data		
E_{Ryd} (eV)	E_{Ryd} (cm^{-1})	n^*	[5] (cm^{-1})	[9] (eV)[a]	[11](eV)
1. $2e \rightarrow nsa_1$					
			Part (a)		
6.167	49 740	2.008	49 702		6.165
8.026	64 743	2.997	64 683		8.022
8.691	70 098	4.000	70 225		8.710
8.988	72 493	4.960	72 674		9.007
9.164	73 913	6.007	73 910		9.17
9.267	74 743	7.047		9.271[6]	-
9.329	75 242	8.009		9.331[5]	
9.375	75 614	8.973		9.375[2]	
9.408	75 881	10.114		9.404[7]	
9.429	76 050	11.032		9.429°	
9.446	76187	11.967		9.447[1]	
9.459	76 291	12.905		9.460[9]	
9.470	76 381	13.882		9.471[7]	
9.480[2]	76 463	14.959		9.481[6]	
9.488[4]	76 529	16.083		9.488[5]	
9.493[5]	76 570	16.924		[9.491[9]][c]	
9.498[4]	76 610	17.871		[9.498[4]][c]	
9.502[4]	76 642	18.774		[9.502°][c]	
9.507[0]	76 679	20.004		9.506[8]	
9.509[6]	76 700	20.816		[9.508[4]][c]	
9.512[1]	76 720	21.698			
9.515[2]	76 745	22.964			
			Part (b)		
6.779	54 676	2.005	54 645		6.777
8.657	69 823	3.005	69 784		8.652
9.312	75 106	3.997	75 131	9.318[6]	9.329
9.619	77 582	5.049	77 700	9.622[6]	9.634
9.784	78 913	6.042	78 989	9.787[4]	9.793
9.887	79 744	7.035		9.882[5]	9.89
9.951	80 260	8.045		9.948[7]	
9.995	80 615	9.040		9.998[5]	
10.028	80 881	10.017		10.029[1]	
10.052	81075	11.027		10.052[7]	
10.070	81220	12.037		10.070[5]	
10.084	81333	13.074		10.084[4]	
10.095[5]	81426	14.093		10.095[3]	
10.103[6]	81491	15.008		10.102[9]	
10.110[7]	81548	15.977		10.110[8]	
10.116[6]	81596	16.942			
10.121[0]	81631	17.788			
10.124[7]	81661	18.606			
10.129[2]	81698	19.773			
10.132[5]	81 724	20.783			
10.134[8]	81 742	21.586			
10.137[0]	81 760	22.448			
10.138[9]	81 776	23.282			
2. $2e \rightarrow npa_1$					
Part (a)					
7.309	58 951	2.469	58 893		7.306
8.415	67 871	3.499	67 987		8.429
8.867	71517	4.495	71480		8.869

Table 2 continued

This work			Literature data		
E_{Ryd} (eV)	E_{Ryd} (cm^{-1})	n^*	[5] (cm^{-1})	[9] (eV)[a]	[11] (eV)
9.089	73 308	5.484	73 314		9.090
9.214	74 316	6.446	74 460		9.215
9.294	74 961	7.417		9.291°	
9.348	75 397	8.394		9.350°	
9.395[1]	75 777	9.399		9.389[3]	
9.419[7]	75 975	10.591		9.421[4]	
9.438[7]	76128	11.532		9.440°	
9.453[3]	76 246	12.448		9.454[9]	
(9.465[1])[b]	76 341	13.406		9.466[7]	
9.474[1]	76 414	14.423		9.476[2]	
9.482[2]	76 479	15.290		9.483[7]	
9.490[3]	76 544	16.285		9.490[2]	
9.495[1]	76 583	17.217		9.493[3]	
(9.500[7])[b]	76 628	18.374		9.499[8]	
9.504[1]	76 656	19.202		9.503[6]	
(9.505[2])[b]	76 665	19.495		9.505[3]	
9.508[4]	76 690	20.429		9.508[7]	
9.511[3]	76 714	21.403		9.511[1]	
Part (b)					
7.956	64169	2.506	63 980		7.996
9.046	72 961	3.489	72 993		9.047
9.486	76 510	4.502	76 482	9.490[2]	9.490
9.711[0]	78 325	5.480	78 308	9.715[7]	9.713
9.840[0]	79 365	6.487	79 365	9.843[8]	9.840
9.922[3]	80 029	7.503		9.920[0]	9.923
9.976[6]	80 467	8.521		9.977[2]	
10.013[8]	80 767	9.517		[10.013[9]][c]	
10.040[8]	80 984	10.509		[10.041[0]][c]	
10.061[3]	81 150	11.510		[10.061[9]][c]	
10.076[7]	81274	12.484		[10.077[6]][c]	
10.089[2]	81375	13.487		10.089[9]	
10.099[2]	81456	14.490		10.099[9]	
10.107[7]	81524	15.545		10.106[7]	
10.114[7]	81581	16.612		10.116[0]	
10.119[9]	81623	17.565		10.120[4]	
10.123[4]	81651	18.306			
10.128[7]	81693	19.367			
10.131[8]	81 718	20.556			
10.134[0]	81 736	21.296			
10.136[3]	81 755	22.203			
10.138[9]	81 776	23.282			
10.140[4]	81 788	24.011			
10.143[3]	81811	25.637			
10.144[5]	81 821	26.414			
10.146[3]	81835	27.725			
10.147[1]	81842	28.374			
10.148[2]	81851	29.345			
3. 2e → *n*pe					
Part (a)					
7.386	59 572	2.513	(59 489)[c]		
8.430	67 992	3.500			{8.429[d]
8.874	71574	4.516			{8.869}[d]
9.089	73 308	5.486			{9.090}[d]
9.217	74 340	6.480			{9.215}[d]
9.296[7]	74 983	7.463		9.297[3]	
9.347[9]	75 396	8.394		9.353[0]	
-	-	-		9.391[2]	

Table 2 continued

This work			Literature data		
E_{Ryd} (eV)	E_{Ryd} (cm^{-1})	n^*	[5] (cm^{-1})	[9] (eV)[a]	[11] (eV)
-	-	-		9.417^{0}	
-	-	-		9.439^{1}	
-	-	-		9.455^{2}	
(9.465^{9})[b]	76 348	13.460		9.469^{4}	
9.476^{3}	76 431	14.501		9.478^{6}	
9.485^{1}	76 503	15.601		9.487^{3}	
9.491^{3}	76 553	16.545		9.488^{5}	
9.496^{7}	76 596	17.525			
(9.500^{7})[b]	76 628	18.374			
(9.505^{2})[b]	76 665	19.495			
Part (b)					
8.000	64 524	2.507	(64 475)[c]		{7.996}[d]
9.062	73 090	3.514			{9.047}[d]
9.493	76 566	4.503			{9.490}[d]
9.715^{5}	78 361	5.508		9.721^{3}	{9.713}[d]
9.842^{0}	79 381	6.500		9.847^{6}	{9.840}[d]
9.922^{4}	80 029	7.504		9.920^{0}	{9.923}[d]
9.974^{4}	80 449	8.471		9.977^{2}	
10.009^{8}	80 734	9.393		[10.013^{9}][c]	
10.040^{0}	80 978	10.474		[10.041^{0}][c]	
10.075^{6}	81265	12.406		[10.077^{6}][c]	
10.087^{7}	81363	13.354			
10.099^{2}	81456	14.490			
4. 2e → *n*da$_1$					
Part (a)					
7.821	63 081	2.812			7.820
8.619	69 517	3.841			8.610
8.949	72 179	4.793			8.949
9.138	73 703	5.813			9.143
9.248^{1}	74 591	6.815	75 590	9.252^{6}	9.253
9.315^{8}	75 137	7.773	75 125	9.318^{9}	9.315
9.367^{5}	75 554	8.855	75 510	9.369^{1}	9.364
9.400^{1}	75 817	9.827	75 780	9.401^{3}	9.396
9.424^{2}	76 011	10.793	75 990	9.425^{5}	9.421
9.442^{2}	76156	11.735	76145	9.443^{6}	9.439
9.456^{8}	76 274	12.711	76 260	9.458^{5}	9.454
9.468^{3}	76 367	13.680	76 345	[9.469^{4}][c]	
9.478^{9}	76 452	14.802		[9.478^{6}][c]	
9.486^{7}	76 515	15.829		[9.485^{8}][c]	
9.493^{3}	76 569	16.889		[9.493^{3}][c]	
9.498^{3}	76 609	17.850		[9.498^{4}][c]	
9.502^{5}	76 643	18.799		[9.502^{0}][c]	
Part (b)					
8.430	67 992	2.801			8.536
9.214	74 316	7.784			9.273
9.575	77 228	4.805			9.593
9.755	78 679	5.768			9.755
9.873^{8}	79 638	6.847	79 617		9.867
9.942^{9}	80195	7.836	80187		9.939
9.985^{2}	80 536	8.723	80 573		9.987
10.020^{0}	80 817	9.795	80 847		10.023
10.045^{9}	81026	10.733	81049	9.580^{4}	10.047
10.064^{5}	81 176	11.694	81202	9.757^{4}	10.064
10.080^{0}	81301	12.780	81320	9.868^{3}	10.08
10.092^{2}	81399	13.776	81414	9.937^{0}	10.092
				9.985^{8}	

Published in : Chemical Physics (2009), vol 365, iss. 3, pp109-128
Status: Postprint (Author's version)

Table 2 continued

This work			Literature data		
E_{Ryd} (eV)	E_{Ryd}(cm ')	n^*	[5] (cm^{-1})	[9] (eV)[a]	[11] (eV)
				10.020[4]	
				10.046[5]	
				10.065[3]	
				10.080[4]	
				10.092[7]	
10.101[4]	81473	14.743		10.101[8]	
10.109[9]	81542	15.858		10.109[6]	
10.115[5]	81587	16.749		10.116[0]	
10.121[0]	81631	17.788		10.121[0]	
10.124[7]	81661	18.612			
10.128[4]	81691	19.549			
10.132[5]	81 724	20.783			
10.134[8]	81 743	21.586			
10.137[0]	81 760	22.448			
10.140[4]	81 788	24.011			
10.142[6]	81806	25.215			
10.146[3]	81835	25.725			
5. 2e → *n*de					
Part (a)					
8.133	65 597	3.109			
8.731	70 420	4.098			
9.013	72 695	5.074			
9.172	73 977	6.071			
9.274	74 800	7.132		9.275[9]	
9.332	75 267	8.066		9.333[0]	
9.378	75 639	9.122		9.371[2]	
Part (b)					
8.713	70 275	3.063			
9.337	75 308	4.055		9.341[6]	
9.632[2]	77 689	5.081		9.635[9]	
9.794[3]	78 996	6.128		9.796[4]	
9.891[0]	79 776	7.065		9.893[5]	
9.953[3]	80 279	8.074		9.956[3]	
9.997[8]	80 637	9.051		9.998[5]	
10.032[7]	80 919	10.126		10.029[1]	
10.051[8]	81073	11.027		10.050[7]	{10.047}[d]
10.070[1]	81221	12.037		10.070[7]	{10.064}[d]
10.084[4]	81336	13.074		[10.084[4]][c]	{10.08}[d]
10.095[5]	81426	14.093		10.097[9]	{10.092}[d]
10.105[1]	81503	15.199		10.106[7]	
(10.116[9])[b]	81598	16.749		[10.116[0]][c]	
6. 2e → *n*f					
Part (a)					
8.663	69 872	3.937			
8.974	72 380	4.898			
9.158	73 864	5.962			
9.254[1]	74 639	6.929		9.258[3]	
9.325[8]	75 218	7.942		9.328[4]	
9.370[5]	75 578	8.946		9.373[1]	
Partb					
9.280[2]	74 850	3.924		9.284[5]	
9.603[6]	77 458	4.933		9.607[4]	
9.776[4]	78 852	5.923		9.779[4]	
9.879[8]	79 686	6.919		9.882[0]	
9.946[5]	80 224	7.915		9.944[1]	
9.990[6]	80 580	8.915		9.991[2]	
10.025[4]	80 860	9.897		10.025[7]	

10.049[2]	81052	10.891	10.049[3]
10.067[2]	81 197	11.886	[10.068[1]][c]
10.082[2]	81318	12.897	10.082[5]
10.093[3]	81 408	13.872	10.093[6]
10.103[2]	81488	14.959	[10.102[9]][c]
10.110[6]	81547	15.962	[10.110[8]][c]
10.116[9]	81598	16.996	[10.116[0]][c]

[a] Foreign data handling procedure: for detailed explanation see text.
[b] Data in brackets: at least two possible assignments.
[c] Data in square brackets: for explanation, see text.
[d] Data in braces are alternative fittings to the data of Ref. [11].

Fig. 7 shows five portions of the photoabsorption spectrum of CH_2DI observed at high resolution with the 3 m-NIM or 10 m-NIM monochromator. Assignments of the abundant fine structure and the energy position of these features are introduced in this figure and listed in Table 4.

4. DISCUSSION OF THE EXPERIMENTAL DATA

The molecular orbital configuration of CH_3I in the C_{3v} symmetry group is

$$I(1s^2 2s^2 2p^6) - C(1s^2) - I(3s^2 3p^6 3d^{10} 4s^2 4p^6 4d^{10})(1a_1)^2 (2a_1)^2 - (1e)^4 (3a_1)^2 (2e)^4 : \tilde{X}^1A_1$$

where the first atomic-like orbitals correspond to the inner-shell orbitals localized on the iodine and carbon atoms. The group of the $1a_1$ and $2a_1$ orbitals are classified as inner-valence shell orbitals whereas the le, $3a_1$, and 2e orbitals have outer-valence shell character.

Fig. 4. *The vacuum UV photoabsorption spectrum of CD_3I in the 5-11 eV photon energy range recorded with the 1.5 m-NIM. The main vibrationless Rydberg transitions and their respective convergence limit are indicated by vertical bars.*

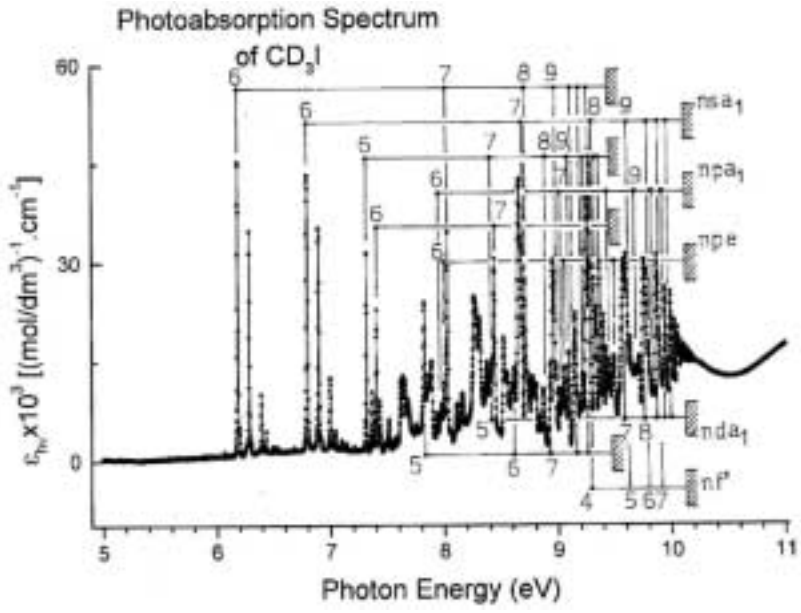

The most accurate and well-resolved He-I photoelectron spectrum [30] provided adiabatic ionization energies at 9.540 ± 0.004 eV, 11.949 ± 0.007 eV and 13.9 eV. They correspond to the ionization of the 2e, $3a_1$ and le orbitals, respectively. The ^2E ground state of CH_3I^+ shows a spin-orbit splitting of 0.628 ± 0.008 eV between its $^2E_{3/2}$-$^2E_{1/2}$ components [28]. The spin-orbit splitting between the $^2P_{3/2}$-$^2P_{1/2}$ states in the free iodine

atom is 0.943 eV [30] whereas it is 1.306 eV in the isoelectronic Xe^+ ion [32]. It is noteworthy that in the HI^+ cation the same coupling has a value of 0.657 eV [33] separating the $X(^2\prod_{3/2}-^2\prod_{1/2})$ components of the ground ionic state.

Excited states of CH_3I^+ are characterized by vertical ionization energies at 12.8 eV and 14.7-15.4 eV corresponding to the $3a_1^{-1}$ and $1e^{-1}$ ionization [30] as measured by He-I photoelectron spectroscopy. Additionally, using the He-II resonance line at 30.4 nm (40.8 eV), Von Niessen et al. [34] observed vertical ionization energies at 12.5 eV, 14.7-15.4 eV, 19.5-21.5 eV and 23.2 eV assigned to $3a_1^{-1}$, $1e^{-1}$, $2a_1^{-1}$ and $1a_1^{-1}$ ionization successively.

Fig. 5*. The vacuum UV photoabsorption spectrum of CD_3I: (a) in the 8.58-9.04 eV range with the 3 m-NIM, 2400 ℓ/mm Pt-grating, $S_{entr} = S_{exit} = 50$ µm, p = 32 µbar; (b) in the 9.20-9.45 eV, (c) in the 9.460-9.521 eV, (d) in the 9.520-9.840 eV and (e) 9.860-10.170 eV ranges with the 10 m-NIM, 1 200 ℓ/mm Pt-grating, $S_{entr} = S_{exit} = 5$ µm, p = 38 µbar. The assignments proposed in this work are included in this figure.*

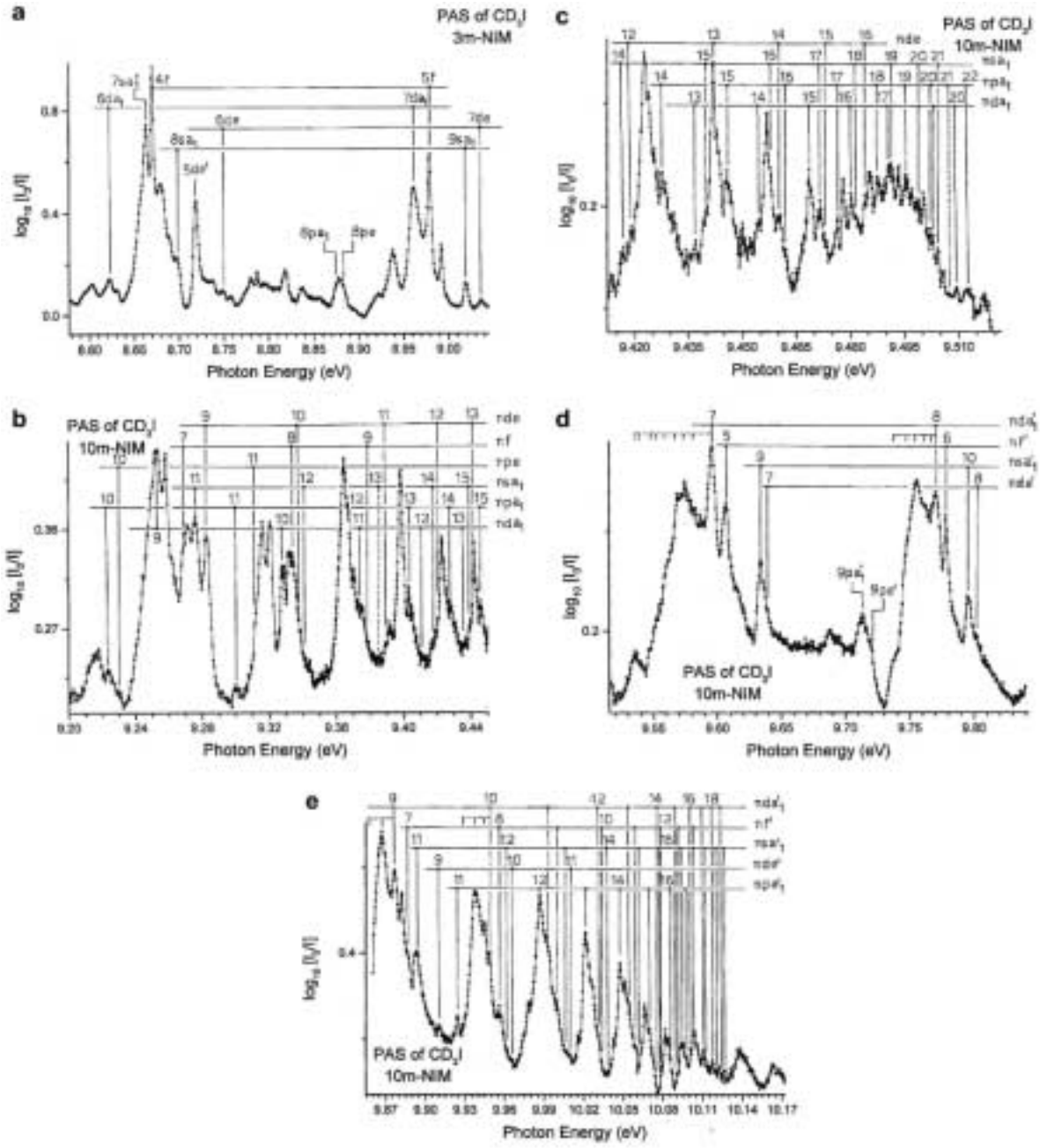

Published in : Chemical Physics (2009), vol 365, iss. 3, pp109-128
Status: Postprint (Author's version)

***Table 3**: Vibrationless Rydberg transitions as observed in CD_3I in the present work converging to both spin-orbit components of the $CD_3I^+(X)$ state: parts (a) and (b) converge to the $^2E_{3/2}$ and $^2E_{1/2}$ ionic states, respectively. Assignments and effective quantum numbers are included (1 eV= 8065.545 cm^{-1} [29]).*

E_{Ryd} (eV)	E_{Ryd}(cm ')	n^*
1. $2e \rightarrow ns a_1$		
Part (a)		
6.185	49 885	2.010
8.033	64 790	2.993
8.698	70154	3.991
9.019	72 743	4.951
9.179	74 034	6.047
9.276	74 816	7.021
9.338^3	75 318	8.049
9.416^2	75 946	10.002
9.439^7	76136	10.973
9.457^7	76 282	12.011
9.471^6	76 394	12.960
9.482^1	76 478	13.941
9.491^4	76 553	14.984
$[9.498^7]^a$	76 612	15.977
$[9.504^2]^a$	76 657	16.871
Part (b)		
6.798	54 830	2.008
8.663^5	69 876	3.002
9.321^8	75 185	4.012
9.633^8	77 702	5.023
9.795^2	79 004	6.001
9.893^6	79 797	6.978
9.961^5	80 345	8.021
10.005^3	80 698	9.007
10.038^0	80 962	10.039
10.061^5	81 151	11.046
10.078^9	81292	12.024
10.093^2	81407	13.057
$[10.103^3]^a$	81489	13.971
10.112^6	81564	15.009
10.119^7	81620	15.977
$[10.126^0]^a$	81672	17.014
$[10.131^0]^a$	81 712	17.999
10.136^3	81 755	19.254
2. $2e \rightarrow np a_1$		
Part (a)		
7.316	59 008	2.467
8.424	67 944	3.473
8.870	71541	4.467
9.093	73 340	5.444
9.224	74 397	6.441
9.302	75 028	7.382
9.366	75 542	8.553
9.398	75 800	9.399
9.425^5	76 022	10.371
9.448^2	76 205	11.449
9.462^1	76 317	12.302
9.476^3	76 432	13.406
9.487^5	76 522	14.524
9.495^1	76 582	15.463
9.502^6	76 644	16.596

9.512^{2}	76 721	18.489

Table 3 *(continued)*

E_{Ryd} **(eV)**	E_{Ryd}**(cm ')**	n^*
Part (b)		
7.976	64 331	2.489
9.058	73 058	3.493
9.497	76 598	4.486
9.715	78 357	5.450
9.845	79 402	6.437
9.924^{3}	80 045	7.396
9.987^{0}	80 548	8.546
10.021^{2}	80 826	9.467
10.047^{1}	81069	10.396
10.069^{6}	81217	11.471
10.085^{2}	81342	12.448
10.097^{5}	81442	13.424
3. $2e \rightarrow n$pe		
Part (a)		
7.401	59 693	2.515
8.442	68 089	3.501
8.884	71654	4.513
9.089	73 308	5.468
9.231	74 453	6.510
9.311	75 098	7.514
Part (b)		
8.022	64 702	2.515
9.069	73 146	3.510
9.504	76 655	4.510
9.720	78 397	5.480
9.853	79 470	6.520
4. $2e \rightarrow nda_1$		
Part (a)		
7.823	63 097	2.805
8.621	69 533	3.823
8.969	72 340	4.831
9.153	73 822	5.838
9.254	74 637	6.755
9.328	75 235	7.811
9.376	75 622	8.780
9.411	75 905	9.806
9.435^{3}	76102	10.797
9.454^{3}	76 254	11.801
9.468^{6}	76 369	12.772
9.480^{1}	76 462	13.756
9.490^{6}	76 547	14.886
$[9.498^{7}]^{a}$	76 612	15.977
$[9.504^{2}]^{a}$	76 657	16.871
9.509^{4}	76 698	17.871
Part (b)		
8.442	68 089	2.804
9.216^{6}	74 332	3.772
9.595^{8}	77 395	4.855
9.770^{2}	78 802	5.812
9.876^{6}	79 660	6.792
9.948^{9}	80 243	7.794
9.993^{5}	80 603	8.706
10.031^{2}	80 907	9.711
10.054^{5}	81095	10.715
10.075^{8}	81267	11.831
10.089^{2}	81375	12.742

l0.l00[6]	81467	13.708

Table 3 *(continued)*

E_{Ryd} (eV)	E_{Ryd}(cm ')	n^*
10.110[7]	81548	14.778
10.117[3]	81602	15.629
10.124[8]	81662	16.801
10.130[2]	81 706	17.829
5. 2e → nde		
Part (a)		
8.150	65 734	3.115
8.748	70 557	4.113
9.025	72 792	5.081
9.192	74138	6.148
[9.282[9]][a]	74 872	7.097
9.341[0]	75 340	8.030
9.389[0]	75 727	9.136
9.419[2]	75 971	10.122
9.442[0]	76155	11.121
9.460[7]	76 305	12.161
9.472[8]	76 403	13.123
9.484[1]	76 494	14.145
Part (b)		
8.718	70 315	3.058
9.364[9]	75 533	4.103
9.639[2]	77 745	5.049
9.801[7]	79 056	6.053
9.902[5]	79 869	7.092
9.965[4]	80 376	8.095
10.008[9]	80 727	9.106
6. 2e → *n*f		
Part (a)		
8.671	69 936	3.950
8.979	72 420	4.911
9.164	73 896	5.907
9.269	74 750	6.934
9.334	75 284	7.900
9.379[4]	75 650	8.904
Part (b)		
[9.282][a]	74 867	3.908
9.607	77 486	4.903
9.779	78 869	5.873
9.886[6]	79 741	6.892
9.956[0]	80 301	7.918
9.999[8]	80 654	8.863
10.033[2]	80 923	9.865
10.059[2]	81 133	10.934
10.077[3]	81279	11.923
10.090[9]	81389	12.873
[10.103[3]][a]	81489	13.971
10.111[8]	81557	14.910
10.118[1]	81608	15.742
[10.126[0]][a]	81672	17.014
[10.131[0]][a]	81 712	17.999

[a] Data in square brackets: at least two possible assignments.

4.1. The Rydberg series analysis

The photoabsorption spectrum displayed in Fig. la clearly shows two very distinct parts: (i) the low

energy part spread over the 5-10 eV photon energy range is very richly structured and (ii)the high energy portion spread over the 10-20 eV photon energy range shows weak or very weak broad bands. These structures could be considerably enhanced by the subtraction procedure as displayed in Fig. lb. To assign these features, their energy positions E_{Ryd} were fitted to the Rydberg formula (1)

$$E_{\mathrm{Ryd}} = \mathrm{IE} - \frac{R}{(n-\delta)^2} = \mathrm{IE} - \frac{R}{(n^*)^2} \qquad (1)$$

where the Rydberg constant is given by R = 13.60569 eV [29], δ is the quantum defect, n^* is the effective quantum number and IE is the convergence limit of the considered Rydberg series, i.e., the associated ionization energy. The lowest value of the principal quantum number n is conventionally taken to be n = 6 for πs- and np-, n = 5 for nd- and n = 4 for nf-type Rydberg orbitals.

Fig. 6. *The vacuum UV photoabsorption spectrum of CH_2DI in the 5-11 eV photon energy range recorded with the 3 m-NIM. The main vibrationless Rydberg transitions and their respective convergence limit are indicated by vertical bars.*

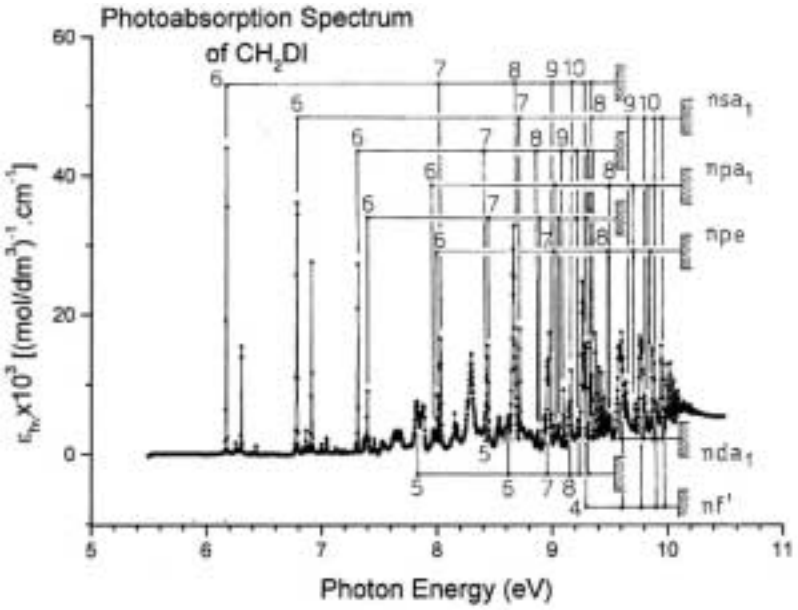

A more accurate formula has been used in earlier works [18,21] taking into account exchange interactions and spin-orbit coupling. Three effects play indeed a role for 2e → nl Rydberg transitions: (i) spin orbit coupling, (ii) exchange interactions and (ii) Jahn-Teller distortion. The latter effect has been shown to be small, leading to a stabilization energy of only 17 meV, as will be discussed in a forthcoming paper [24]. In CH_3I, exchange interactions are small compared to the spin-orbit splitting so that the lowest Rydberg members can already be described by Hund's case (c). The simple Rydberg formula can than be applied to the series converging to, respectively, the $^2E_{3/2}$ and $^2E_{1/2}$ of CH_3I^+.

4.2. The high energy region (10-20 eV)

The energy positions of the structures observed in this photon energy range are listed in Table 1 together with the data from Ref. [13] evaluated as described in Section 2.2. A reasonable agreement is found between the results of both experiments. However, Olney et al. [13] did not suggest any interpretation. Assignments and convergence limits are proposed in Table 1.

The first and most intense peak in Fig. lb is located at 11.00 eV. This feature spreads overthe energy range 10.5-11.5 eV.A3a_1 → 7s transition is the most likely assignment. Using formula (1) an effective quantum number n^* = 3.03 is derived. It is noteworthy that the full-width of this structure is about 1 eV, very similar to the width of the $\tilde{A}^2A_1$ ionic state (convergence limit) of CH_3I^+ as observed in the He-I photoelectron spectrum by Karlsson et al. [30].

Published in : Chemical Physics (2009), vol 365, iss. 3, pp109-128
Status: Postprint (Author's version)

Fig. 7. *The vacuum UV photoabsorption spectrum of CH_2DI: (a) in the 8.60-9.07 eV, (b) in the 9.20-9.45 eV and (c) in the 9.420-9.520 eV ranges with the 3 m-NIM, 2400 ℓ/ mm Pt-grating, $S_{entr} = S_{exit} = 30$ µm, p = 34 µbar: (d) in the 9.550-9.850 eV and (e) in the 9.840-10.180 eV ranges with the 10 m-NIM, $S_{entr} = S_{exit} = 10$ µm, p = 35 µbar. The assignments proposed in this work are included in this figure.*

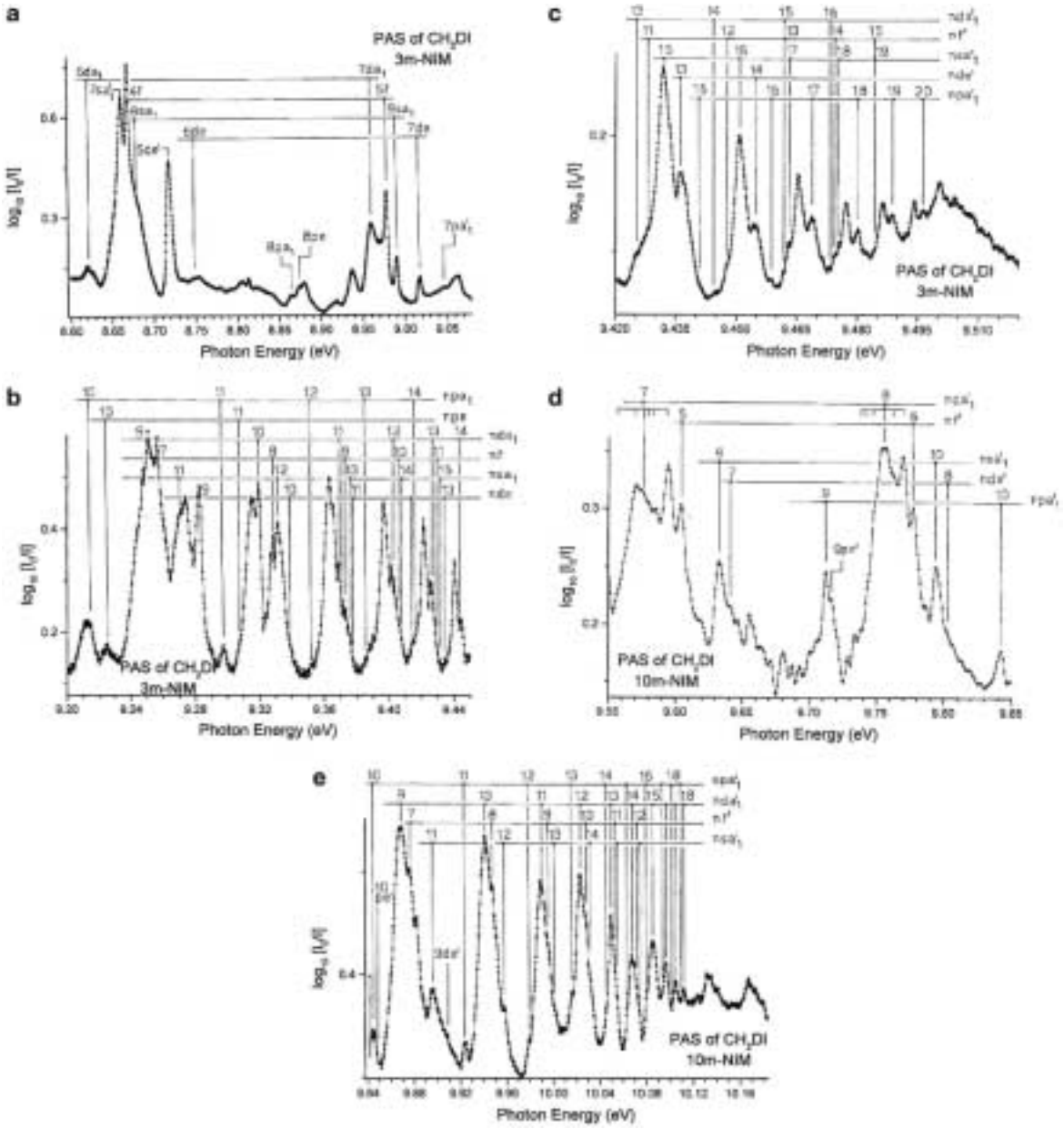

The next three features at 11.68 eV, 12.69 eV and 13.78 eV converge to the le^{-1} ionization limit. The corresponding ^2E ionic state is Jahn-Teller split with a much larger stabilization energy than for the ground state [35]. The lowest energy structure at 11.68 eV could only be assigned to a le → ($^2E_{3/2}$)6s transition characterized by n^* = 2.12. The two following features, respectively, at 12.69 eV and 13.78 eV could be considered as generated by le → ($^2E_{3/2}$)6p and le → ($^2E_{3/2}$)6d transitions. Effective quantum numbers n^*(6p) = 2.61 and n^*(6d) = 3.89 are derived. Alternatively, these energies could be assigned to le → ($^2E_{1/2}$)6s and le → ($^2E_{1/2}$)5d transitions. In this case effective quantum number values n^*(6s) = 2.24 and n^*(5d) = 2.90 are obtained.

Between 14.5 eV and 20 eV the Δ-plot in Fig. lb is fairly flat oscillating about zero. When significant, very weak structures could be mentioned at about 15.8 eV and 18.4 eV. A similar feature is found in the dipole (e, e) spectrum of CH_3I at 16.4 eV [13]. Inserting E_{Ryd} = 15.8 eV in Eq. (1) and using n^*(ns) = 2.03, one obtains

IE = 19.2 eV (dotted lines in Fig. lb). A $2a_1 \rightarrow ns$ transition could thus be involved. The He-II photoelectron spectrum [34] shows a band peaking at about 19.5 eV. The TPES [35] of CH_3I shows a very weak (about 0.8% of the $\tilde{X}\,^2E_{3/2}(v= 0)$ intensity) complex structure with several "bands" spread between 18.6 eV and 23.0 eV. This could correspond to a manifold of single and doubly excited ionic states.

The present observations and our attempts for their interpretation are summarized in Fig. 8.

Table 4: *Vibrationless Rydberg transitions as observed in H_2CDI in the present work and converging to both spin-orbit components of the H_2CDI^+ (X) state: parts (a) and (b) converge to the $^2A'$ and $^2A''$ ionic states, respectively. Assignments and effective quantum numbers are included (1 eV= 8065.545 cm^{-1} [29]).*

E_{Ryd} (eV)	E_{Ryd}(cm^{-1})	n^*
1. $2e \rightarrow nsa_1$		
Part (a)		
6.172	49 781	2.009
8.031	64 774	2.999
8.681	70 017	3.971
8.990	72 509	4.960
9.164	73 913	5.984
9.271	74 776	7.060
9.330^{6}	75 256	7.985
9.375^{5}	75 619	8.986
$[9.406^{9}]^a$	75 864	9.962
9.431^{7}	76 072	10.973
9.450^{6}	76 224	12.069
9.463^{6}	76 329	13.001
9.474^{8}	76419	14.022
$[9.483^{2}]^a$	76 487	14.959
Part (b)		
6.784	54 717	2.005
8.661	69 856	3.005
9.318^{7}	75160	4.002
9.632^{5}	77 691	5.041
9.794^{8}	79 000	6.032
9.895^{3}	79 811	7.063
9.957^{9}	80 316	8.047
10.000^{5}	80 659	9.013
10.031^{0}	80 905	9.966
10.055^{5}	81103	10.997
10.074^{3}	81255	12.050
2. $2e \rightarrow npa_1$		
Part (a)		
7.315	58 999	2.471
8.418	67 896	3.476
8.864	71493	4.473
9.093	73 340	5.492
9.214^{2}	74 317	6.423
9.297^{1}	74 986	7.423
9.352^{8}	75 435	8.436
9.387^{5}	75 515	9.324
9.415^{0}	75 937	10.270
9.441^{1}	76148	11.493
9.458^{3}	76 286	12.577
9.468^{6}	76 369	13.433
9.480^{3}	76 464	14.614
9.488^{6}	76 531	15.671
9.496^{3}	76 592	16.888
Part (b)		
7.971	64 290	2.488
9.046	72 961	3.482

Published in : Chemical Physics (2009), vol 365, iss. 3, pp109-128
Status: Postprint (Author's version)

9.494^{2}	76 576	4.494
9.712^{7}	78 338	5.467
9.844^{4}	79 400	6.484
9.923^{8}	80 041	7.464
9.978^{9}	80 485	8.482
10.016^{7}	80 790	9.483
10.045^{4}	81022	10.534

Table 3 *(continued)*

E_{Rvd} **(eV)**	E_{Rvd}**(cm^{-1})**	***n****
10.063^{1}	81164	11.389
10.081^{1}	81310	12.513
10.093^{0}	81405	13.469
10.102^{9}	81485	14.457
10.110^{2}	81544	15.342
3. 2e → *n*pe		
Part (a)		
7.398	59 669	2.518
8.427	67 568	3.490
8.876	71590	4.513
9.098^{9}	73 388	5.529
9.225^{6}	74 409	6.537
9.306^{6}	75 063	7.570
9.355^{4}	75 456	8.493
9.390^{2}	75 737	9.406
Part (b)		
8.004	64 557	2.507
9.062^{8}	73 096	3.509
9.499^{0}	76 615	4.510
9.716^{5}	78 369	5.489
9.847^{3}	79 424	6.513
4. 2e → nda_1		
Part (a)		
7.827	63 129	2.815
8.621	69 533	3.839
8.959^{4}	72 262	4.824
9.149^{3}	73 794	5.871
9.250^{4}	74 609	6.807
9.320^{1}	75 172	7.795
9.369^{2}	75 568	8.822
9.401^{5}	75 828	9.771
9.426^{4}	76 029	10.756
9.445^{6}	76184	11.759
[9.461^{9}]	76 315	12.873
9.473^{3}	76 407	13.872
Part (b)		
8.427	67 968	2.796
9.224^{7}	74 402	3.798
9.575^{8}	77 234	4.793
9.756^{9}	78 695	5.753
9.867^{7}	79 588	6.731
9.939^{8}	80170	7.721
9.988^{3}	80 561	8.701
10.021^{8}	80 831	9.647
10.049^{3}	81053	10.706
10.066^{7}	81 193	11.589
10.085^{5}	81345	12.842
10.095^{7}	81427	13.718
10.104^{9}	81501	14.684
5. 2e → *n*de		

Part (a)		
8.154	65 766	3.128
8.749	70 565	4.137
9.017[3]	72 729	5.082
9.179[6]	74 038	6.110
9.273[4]	74 795	7.091
9.336[6]	75 305	8.099

Table 3 *(continued)*

E_{Rvd} (eV)	E_{Rvd} (eV)	E_{Rvd} (eV)
9.377[9]	75 638	9.051
9.412[3]	75 915	10.164
9.434[7]	76 096	11.157
9.452[7]	76 241	12.207
Part (b)		
8.718[2]	70 317	3.063
9.640[7]	77 757	5.080
9.803[7]	79 072	6.111
9.905[9]	79 896	7.205
6. 2e → *n*f		
Part (a)		
8.668[4]	69 915	3.942
8.978[3]	72 415	4.904
9.158°	73 864	5.937
9.256[1]	74 655	6.874
9.328°	75 235	7.936
9.372[8]	75 597	8.915
[9.406[0]][a]	75 864	9.929
9.429[7]	76 056	10.910
9.448[6]	76 213	11.935
[9.461[9]]	76 315	12.873
[9.474[8]][a]	76 419	14.022
[9.483[2]][a]	76 487	14.959
Part (b)		
9.282[4]	74 868	3.919
9.604[2]	77 463	4.912
9.777[2]	78 858	5.900
9.874[9]	79 646	6.813
9.946[8]	80 226	7.843
9.996[4]	80 626	8.904
10.028[6]	80 886	9.879
10.052[9]	81082	10.872
10.072[6]	81241	11.942

[a] Data in square brackets: at least two possible assignments.

4.3. The low energy region (6-10.5 eV): analysis using the Rydberg formula [1]

4.3.1. The methyl-h_3 iodide vacuum UV spectrum

The numerous vibrationless Rydberg transitions observed in the photoabsorption spectrum of CH_3I between 5 eV and 11 eV are identified in Figs. 2 and 3. The energy positions and their assignments are listed in Table 2. These transition energies are classified according to the nature of the involved Rydberg orbital which is based on the value of the effective quantum number n^* . For clarity this classification is subdivided further according to the convergence limits $^2E_{3/2}$ and $^2E_{1/2}$ designated, respectively, by part (a) and part (b) in Table 2. Energy levels corresponding to several possible assignments are listed in square brackets.

Three previous data sets [5,9,11] are included in Table 2 for comparison. When assignments are proposed [5,11] these are included. For large discrepancies in the assignments between the present work and

Refs. [5] and/or [11] the energy levels involved are mentioned in brackets. The data sets from Ref. [9] are obtained by the procedure described in Section 2.2.

Fig. 8. *Energy level diagram of the ground and excited states of the CH_3I^+ cation and the high energy (HE) Rydberg (designated by their nℓ) states of CH_3I observed in this work. Dashed arrows point to their respective convergence limits.*

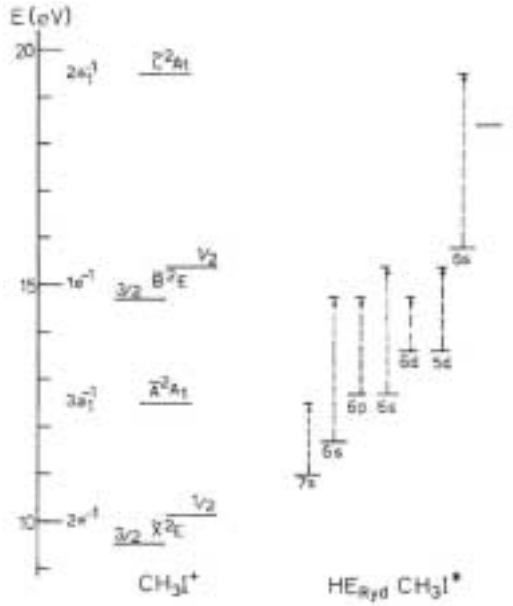

The estimated error on the earlier measurements was not specified by the authors. In the present work, the data being obtained with three monochromators characterized by very different resolution, at low energy (1.5 m-NIM), an error of 2-3 meV (16-24 cm^{-1}) is estimated, whereas for $h\nu \geq 9$ eV (72 000 cm^{-1}) (3 m-NIM or 10 m-NIM) an error of 1 meV (8 cm^{-1}) or better is expected. Therefore, in this photon energy range the energy levels are mentioned at the 100 μeV level.

The best agreement is observed between the present measurements and the data of Price [3]. For the two series reported by this author an average deviation of (20 ±14) cm^{-1} and (-7 ± 23) cm^{-1} is calculated. Comparing with the data published by Hochmann et al. [5] deviations are generally of the order of (-20 ± 60) cnr^1 probably lying in the overlapping error limits. However, a few deviations of -100 to -180 cm^{-1} have to be mentioned. In these cases the discrepancy could be attributed to assignment differences.

For the assignments deduced in the present work and listed in Table 2, adiabatic ionization energies (IE_{ad}) values of CH_3I are needed. Several accurate values are proposed in the literature, i.e., $IE_{ad}(\tilde{X}\,^2E_{3/2})$ = 9.540 ± 0.004 eV and $IE_{ad}(\tilde{X}\,^2E_{1/2})$ = 10.168 ± 0.004 eV are measured by He-I photoelectron spectroscopy [30]. By Rydberg series extrapolation 76 930 cm^{-1} and 81 990 cm^{-1} are obtained by Price [3], or 9.538 ± 0.002 eV and 10.165 ± 0.002 eV using the IUPAC recommended eV/cm^{-1} conversion factor [29]. The author himself [3] reported the energies of 9.490 ± 0.002 eV and 10.115 ± 0.002 eV. By the same method Baig et al. [9] proposed 76 930.0 ± 1 cm^{-1} and 81 979.0 ± 1 cm^{-1}, i.e., 9.5381 ± 0.0001 eV and 10.1641 ± 0.0001 eV. By zero kinetic energy (ZEKE) spectroscopy [36] of a CH_3I/Ar molecular beam, $IE_{ad}(\tilde{X}\,^2E_{3/2})$ = 76 934 ± 5cm^{-1} (9.5386 ±0.0006 eV) and $IE_{ad}(\tilde{X}\,^2E_{1/2})$ = 81 983 ± 5 cm^{-1} (10.1646 ± 0.0006) eV have been measured. In an ongoing photoelectron spectroscopic work [31] we obtained 9.541 ± 0.005 eV or 76 953 ± 40 cm^{-1} and 10.164 ± 0.005 eV or 81 978 ± 40 cm^{-1}. Owing to the good agreement for the $IE_{ad}(\tilde{X}\,^2E_{3/2})$ (within 0.003 eV) and for the $IE_{ad}(\tilde{X}\,^2E_{1/2})$ (within 6 μeV), later in this work, as we need ionization energy data for the deuterated species CD_3I and CH_2DI, we will adopt the latter photoelectron spectroscopic data obtained in our laboratory for self-consistency.

The two lowest energy photoabsorption bands are assigned to $2e \rightarrow 6sa_1$ Rydberg transitions. These transitions are also observed in CH_3C1 [17] and in CH_3Br [20]. Several of their characteristics show a continuous evolution along the halogen series: (i) the intensity of these transitions with respect to the first $2e \rightarrow npa_1$ is weak in CH_3Cl (about 8%), strong in CH_3Br (about 32%) and the strongest in the CH_3I spectrum (about 130%) and (ii)

the width of the bands decreases drastically from CH_3Cl to CH_3Br and CH_3I where the bands are atomic-line shaped. These observations are valid for both the $2e \rightarrow (^2E_{3/2})6sa_1$ and $2e \rightarrow (^2E_{1/2})6sa_1$ transitions. Consequently, there is no correlation between the projection of the total angular momentum and the intensity or bandwidth. However, they seem both to be related to the halogen atomic number: the higher the Z of the halogen, the stronger the transition and the narrower the bands.

A fairly constant value of the average quantum defect $\delta[(^2E_{3/2})6sa_1] = 4.034 \pm 0.090$ and $5[(^2E_{1/2})6sa_1] = 4.033 \pm 0.12$ is observed. For the latter series this parameter tends to increase for high-π values: for the last members with high-π small term values become inaccurate and so does the quantum defect.

Fig. 9. *Correlation diagrams of $ln[T_n]$ as a function of $ln[n]$ for sa_1- (a), pa_1- (b), da_1- (c) f-type (d), pe- (e) and de-transitions (f) in CH_3I with or without Xe.*

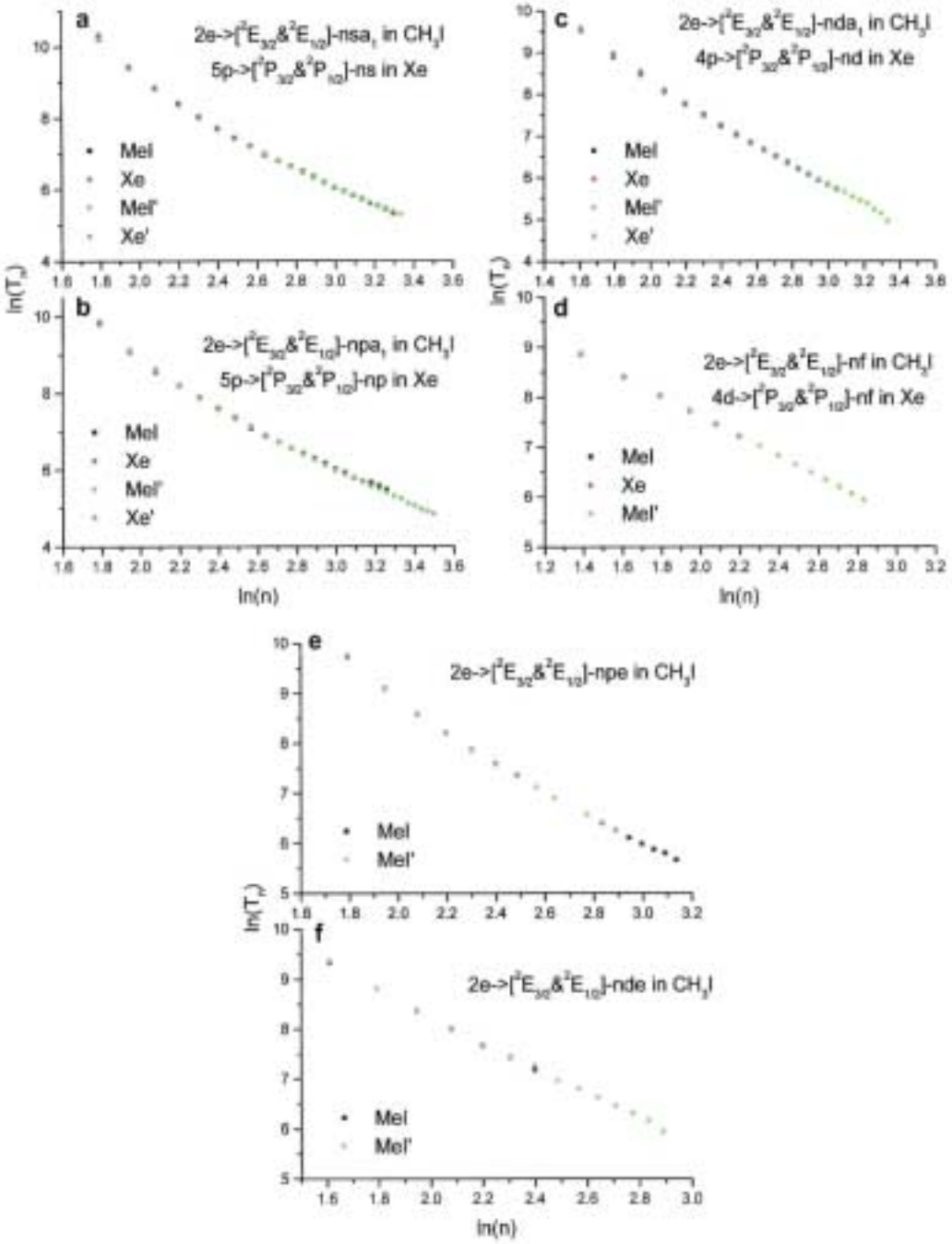

As shown in Table 2, the assignments listed in this work for the first five members of the πs-series and those proposed by Hoch-mann et al. [5] and Eden et al. [11] agree very well. For the higher members ($n > 10$) only the energy levels could be compared to the results of the work of Baig et al. [9]. It has to be reminded that the values listed in column 6 of Table 2 result from the procedure described in Section 2.2. The very good parallelism between the readings from those spectra and the energy levels measured in the present work doesn't imply the same assignments by these authors [9]. The assignments proposed in our work are inserted in Fig. 3.

To confirm these assignments, the close correlation between the term values measured in CH_3I and those observed in the corresponding rare gas will be examined. This comparison was successfully used in the interpretation of the CH_3Br absorption spectrum [21] and by Baig et al. [9] for the *n*s- and *n*d-series assignments in CH_3I. Fig. 9a shows the ln[T_n]-versus-ln[n] diagram for both $2e \rightarrow (^2E_{3/2})nsa_1$ and $2e \rightarrow (^2E_{1/2})nsa_1$ in CH_3I and for the $5p \rightarrow (^2P_{3/2})ns$ and $5p \rightarrow (^2P_{1/2})ns$ in the Xe atom [32]. Over the whole range of n values [n = 6-27(28)] the data overlap. Furthermore, no difference is observed between the two transition types (Ω = 3/2 or 1/2) in neither CH_3I nor Xe.

Contrary to the observation made in the photoabsorption spectra of CH_3C1 [18] and of CH_3Br [21] the $2e \rightarrow npa_1$ no longer dominates the spectrum (see Fig. 2) as it has already been pointed out by Dagata et al. [10]. For the $2e \rightarrow npa_1$ Rydberg transitions, Table 2 shows a fairly constant quantum defect particularly for the first 10-13 terms of these series. An averaged quantum defect $\delta = 3.54 \pm 0.06$ for the $2e \rightarrow (^2E_{3/2})npa_1$ and $\delta = 3.51 \pm 0.09$ for the $2e \rightarrow (^2E_{1/2})npa_1$ are calculated. Within experimental error no difference could be noticed between these two series.

Fig. 9b shows the ln[T_n]-versus-ln[n] diagram related to the $2e \rightarrow npa_1$ transitions in CH_3I and Xe. Up to n = 23 the four data series fully overlap. Only for higher $n > 23$ the two transition series $2e \rightarrow (^2E_{3/2})npa_1$ and $2e \rightarrow (^2E_{1/2})npa_1$ seem to diverge slightly.

However, due to the non-spherical character of the molecular field, the three p-orbitals are split into one a_1 and one doubly degenerate e orbital. These orbitals are, respectively, aligned along and perpendicularly to the C_{3v} axis of the molecule. This fact has already been mentioned earlier [18,21]: Rydberg transitions corresponding to $2e \rightarrow npa_1$ and $2e \rightarrow npe$ have been highlighted in the photoabsorption spectra of CH_3Cl [18] and CH_3Br [21]. The splitting between the $3pa_1$ and the 3pe-orbitals is 393 meV (3170 cm^{-1}) in CH_3Cl [18] and 156 meV (1258 cm^{-1}) in CH_3Br [21].

To find out whether $2e \rightarrow \pi pe$ transitions are present or not, we carefully analyzed the transition intensities and the vibrational structure in the vicinity of the $6pa_1$ band. The photoabsorption spectra of CD_3I and CH_2DI were investigated in the same energy range. As observed in all our previous studies [18,19,21,22] electronic transition energies are "blue-shifted" whereas vibrational transition energies are "red-shifted" by isotopic substitution.

Around 7.3-7.4 eV the spectrum of CH_3I shows four peaks at 7.309 eV, 7.362 eV, 7.387 eV and 7.409 eV successively. The first band is assigned to the $2e \rightarrow (^2E_{3/2})6pa_1$ transition, the second and fourth well-resolved structures are weak and broad whereas at 7.387 eV a strong and sharp band shows up (see Fig. 2). The corresponding energy range has been examined in CH_2DI and in CD_3I where the same sharp and strong band is measured at 7.398 eV and 7.401 eV, respectively. As shown in Tables 3 and 4 the $2e \rightarrow 6pa_1$ transition in CH_2DI and CD_3I has been assigned to the band measured at 7.315 eV and 7.316 eV, respectively. The energy splitting between the $6pa_1$ band and the sharp and strong structure is blue shifted: 0.078 eV (629 cm^{-1}) in CH_3I becomes 0.083 eV (669 cm^{-1}) in CH_2DI and 0.085 eV (686 cm^{-1}) in CD_3I. This is observed for all the other vibrationless Rydberg transitions (see Tables 3 and 4). The weaker and broader structures represent vibrational structure and the associated wavenumbers are red-shifted upon isotopic substitution. This analysis will be the subject of a forthcoming paper [24].

This value of the npa_1-*n*pe splitting in CH_3I has to be compared with the values mentioned above for CH_3C1 and CH_3Br. One observes a drastic decrease of the splitting with increasing the halogen atomic number. For this splitting the "quasi-united atom" model for the CH_3X Rydberg molecule becomes a better representation, the higher the Z of the halogen atom. Ultimately, the pa_1- and pe-orbitals become degenerate as in the Xe atom. This remark remains valid for the $(^2E_{1/2})$npe Rydberg series.

The energy levels of the successive Rydberg $2e \rightarrow npe$ transitions are listed in Table 2 and represented in Figs. 2 and 3. Averaging the quantum defect δ over all the n values, $\delta = 3.51 \pm 0.06$ and $\delta = 3.53 \pm 0.05$ are deduced. These are very close to those obtained for both $2e \rightarrow npa_1$ Rydberg series, i.e., 3.54 ± 0.06 and $3.51 \pm$

0.09. This observation fits in a trend already mentioned for the 2e → πpe transitions in CH_3C1 and CH_3Br. In the former case δ = 0.67 and 0.43 [18] whereas in the latter δ = 0.58 and 0.54 [21] were obtained. This result pinpoints the conclusion drawn above about the "quasi-united atomic" behaviour of the Rydberg states in CH_3I.

Only one literature value is available for this series [5] (see column 4, Table 2): both 59 489 cm^{-1} (7.376 eV) and 64 475 cm^{-1} bands were originally assigned to 2e → πd transitions. Effective quantum numbers n^* = 2.51 and 2.50 were deduced [5].

These two values are compared to the results of the present work. The agreement is fairly good as being within the scattering limits of ±60 cm^{-1} noticed earlier. However, the effective quantum number n^* = 2.513 would lead us to classify this transition as p-type rather than d-type transition. This proposal would agree with the classification reported by Price [3] who let the d-series start at 74 590 cm^{-1}.

For the higher members of these Rydberg transitions, comparable energy levels have been read in the spectrum published by Baig et al. [9]. A few of them were assigned by the authors to 2e → ($^2E_{3/2}$)np transitions (see Fig. 1 in Ref. [9]) without any other comment or specification. Fig. 9e shows the ln[T_n]-versus-ln[n] diagram related to the 2e → ($^2E_{3/2}$ and $^2E_{1/2}$)$n$pe transitions. As already noticed for the nsa_1- and npa_1-series, both πpe series overlap. The assignments suggested in this work are included in the spectra reproduced in Fig. 3.

Table 2 further displays the results of the present work and the data listed in Ref. [3] or read from the spectra reported by Ref. [9] in the literature and related to 2e → nda_1 Rydberg transitions. The energy levels corresponding to these transitions are localized in Fig. 3. With respect to the former the average scattering is about 2.5 meV (about 20 cm^{-1}) and the latter 0.2-4 meV (about 2-32 cm^{-1}). Fig. 9c shows the ln[T_n]-diagram for CH_3I and for Xe: all data points for 2e → ($^2E_{3/2}$ and $^2E_{1/2}$)nda_1 overlap those related to the 5p → ($^2P_{3/2}$ and $^2P_{1/2}$)nd transitions in Xe. This is confirmed by the averaged δ values, i.e., 2.200 ± 0.053 and 2.216 ± 0.041 for the 2e → ($^2E_{3/2}$ and $^2E_{1/2}$)nd transitions, respectively. Within the standard deviation limits the two quantum defects are not distinguishable.

Additionally to eight Rydberg series observed in CH_3Br [21], two more series corresponding to 2e → ($^2E_{3/2}$ and $^2E_{1/2}$)$n\ell$ have been highlighted, where l = 2 or 3. These series were characterized by low (and even negative) δ values. A very good correlation between the term values of these series and those of the 4p → nf transitions in Kr had been demonstrated. However, due to the non-sphericity of the molecular field, we expect the atomic d-orbital to be split in different d-type molecular orbitals, i.e., a_1, e and e orbitals in the C_{3v} symmetry. These transitions should be characterized also by low δ values. Therefore, the additional Rydberg series in CH_3Br couldn't be definitely assigned to $n$de or nf.

In CH_3I four supplementary series are observed. They start at 8.133 eV (65 597 cm^{-1}) and 8.713 eV (70 275 cm^{-1}) for 2e → ($^2E_{3/2}$ and $^2E_{1/2}$)$n\ell$ transitions and at 8.663 eV (69 872 cm^{-1}) and 9.280 eV (74 850 cm^{-1}) corresponding to 2e → ($^2E_{3/2}$ and $^2E_{1/2}$)$n\ell'$ transitions. The lowest effective quantum numbers are n^* = 3.109 and 3.063 and n^* = 3.937 and 3.924, respectively. These transitions have all been located in the spectra reproduced in Fig. 3. These have not been reported earlier.

As shown in Fig. 3, higher resolution spectra clearly confirm these results. Very sharp transitions start at 8.663 eV (69 872 cm^{-1}) and 9.280 eV (74 850 cm^{-1}). Averaged quantum defects δ = 0.056 ± 0.011 and 0.076 ± 0.033 are derived. Fig. 9d shows how these spectroscopic data on CH_3I fit to the 5p →nf (n = 4-9) transitions in Xe. All available data overlap. This result is even more convincing than in CH_3Br [20]: more data are available for Xe [30]. On the basis of these arguments we would suggest to assign these features to 2e → ($^2E_{3/2}$ and $^2E_{1/2}$)nf Rydberg transitions. Examining the spectra displayed in Figs. 1 and 2 in Ref. [9], structures in the corresponding energy ranges (see Fig. 3 in the present work) are roughly assigned to nd transitions only. No more details are reported.

The second additional new pair of Rydberg series start at 8.133 eV (65 597 cm^{-1}) and 8.713 eV (70 275 cm^{-1}) (see Table 2). Members of these are located and designated in Fig. 3 as $n$de and πde' and converge to the $^2E_{3/2}$ and $^2E_{1/2}$ ionization limits, respectively. These series can be described by the averaged δ values δ = 1.905 ± 0.030 and δ = 1.930 ± 0.032.

As mentioned earlier, the atomic d-orbital has to be split into one a_{1}- and two e-type molecular orbitals in the C_{3v} symmetry. The nda_1 Rydberg states being already assigned, we would suggest to assign the present Rydberg levels considered here to 2e → ($^2E_{3/2}$ and $^2E_{1/2}$)$n$de transitions.

4.3.2. The methyl-d_1 and methyl-d_3 iodide vacuum UV spectra

To find a support to our interpretation of the CH_3I vacuum UV photoabsorption spectrum we measured the corresponding data for CD_3I and CH_2DI. Their spectra are reproduced between 5.0 eV and 10.5 eV in Figs. 4 and 6, respectively. More detailed pictures of these spectra are reproduced in Figs. 5 and 7 on an extended photon energy scale. The main structures and their assignments are inserted in these figures. The numerical data related to the energy levels of the numerous vibrationless Rydberg transitions observed in these two molecules have been listed in Tables 3 and 4. For clarity, the classification of the data listed in these tables is the same as that adopted in Table 2.

Before any spectral analysis using Rydberg formula (1), the ionization energies of CD_3I and CH_2DI are required. This quantity has been measured by photoelectron spectroscopy [31]. The He-I pho-toelectron spectrum of the first band of CD_3I has been recorded with 1 meV increments over 1024 channels. A mixture of Ar/Kr/ Xe/Air is introduced simultaneously for the electron energy scale calibration. For CD_3I the two lowest ionization energies were determined at $IE_{ad}(\tilde{X}\,^2E_{3/2}) = 9.552 \pm 0.005$ eV (77 043 ± 40 cm^{-1}) and $IE_{ad}(\tilde{X}\,^2E_{1/2}) = 10.173 \pm 0.005$ eV (82 051 ± 40 cm^{-1}). Using the same technique and procedure $IE_{ad}(\tilde{X}\,^2E_{3/2}) = 9.544 \pm 0.005$ eV (76 978 ± 40 cm^{-1}) and $IE_{ad}(\tilde{X}\,^2E_{1/2}) = 10.168 \pm 0.005$ eV (82 010 ± 40 cm^{-1}) are measured in the CH_2DI He-I photoelectron spectrum. In the literature the only data available for CD_3I has been obtained by ZEKE-photoelectron spectroscopy [36]: the ionization energies of 76 958 ± 5 cm^{-1} and 81 996 ± 5 cm^{-1} are reported. These values are close and inside the error limits. For self-consistency in this work we will use the He-I photoelectron spectroscopic data obtained in our laboratory [31].

To the best of our knowledge the vacuum UV photoabsorption data are available in the literature neither for CD_3I nor CH_2DI in the wavelength region discussed in the present work. The spectroscopic work of Felps et al. [6] dedicated to CD_3I was restricted to the 170-205 nm (6.0-7.3 eV or 48 780-58 823 cm^{-1}) photon wavelength range only. This work was focused on the vibrational analysis of the first two Rydberg states. This same aspect will also be the subject of a forthcoming paper [24].

By investigating the three isotopomers, an important information is the shape of the spectra showing more clearly several parts or details. This is particularly obvious in the spectra reproduced in Figs. 5 and 7 as compared to Fig. 3. All these spectra were obtained in approximately the same experimental conditions. These figures show the complexity of the spectrum e.g., in the 8.60-8.70 eV, 9.20-9.40 eV photon energy ranges. Several peaks are split. These details have never been reported earlier.

As compared to the long $2e \rightarrow nsa_1$ (n = 6-27) Rydberg series in CH_3I, the corresponding series measured in the deuterated isotopomers CH_2DI (n = 6-19) and CD_3I (n = 6-21) are shortened. For most of the transition energies, the "blue-shift" already mentioned in earlier works [18,21] has to be noticed and follows the $E_{Ryd}(CH_3I) < E_{Ryd}(CH_2DI) < E_{Ryd}(CD_3I)$ ranking. The same trend is observed for IE_{ad} of the corresponding molecules measured by Hel-PES. As expected, most of the calculated effective quantum numbers are equal within a few thousandths for many cases. Calculating the averaged quantum defects over all transitions in both the $2e \rightarrow nsa_1$ series, $\delta = 4.006 \pm 0.030$ and $\delta = 3.989 \pm 0.023$ in the case of CD_3I and $\delta = 4.010 \pm 0.030$ and $\delta = 3.970 \pm 0.026$ for CH_2DI. These values have to be compared with $\delta = 4.034 \pm 0.090$ and $\delta = 4.033 \pm 0.12$ for CH_3I. Within the error limits these values are in very good agreement. One could recognize a slight differentiation of both series through their δ values.

Felps et al. [6] observe two vibrationless Rydberg transitions in CD_3I at 49 815 ± 30 cm^{-1} and at 54 740 ±75 cm^{-1}. These values have to be compared with 49 885 ± 20 cm^{-1} and 54 830 ± 20 cnr^{1} measured in the present work. The data in CH_3I related to the $2e \rightarrow nsa_1$ transitions are reported at 49 710 ± 30 cm^{-1} and 54 625 ± 35 cm^{-1}. [6] whereas in the present work (see Table 2) they are measured at 49 760 ± 20 cm^{-1} and 54 676 ± 20 cm^{-1}.. The extent of the discrepancy between the data for CD_3I is unusual and no obvious explanation is at hand.

As already shown in the vacuum UV spectrum of CH_3I both the $2e \rightarrow (^2E_{3/2}, ^2E_{1/2})npa_1$ and the $2e \rightarrow (^2E_{3/2}, ^2E_{1/2})npe$ series are detected up to n = 20 for the former and n = 11 for the latter in CH_2DI and CD_3I. Their transition energies are all shifted to higher energies ("blue-shifted") as compared to CH_3I.

The average quantum defect characterizing the $2e \rightarrow (^2E_{3/2}, ^2E_{1/2})npa_1$ transitions are $\delta = 3.55 \pm 0.06$ and $\delta = 3.53 \pm 0.03$ for CH_2DI and CD_3I. These results can be compared with the average value deduced for the same transitions in CH_3I where $\delta = 3.52 \pm 0.07$ has been determined. This quantity is very stable as has been also experienced for the $2e \rightarrow nsa_1$ transitions. This property remains valid for the $2e \rightarrow (^2E_{3/2}, ^2E_{1/2})npe$ transitions in

the two isotopomers. Average values of δ = 3.49 ± 0.02 for CD_3I and δ = 3.49 ± 0.05 for CH_2DI compare very well to δ = 3.53 ± 0.07 obtained from our analysis in CH_3I.

Finally, a last result of the present Rydberg series analysis in CH_2DI and CD_3I is to prove the observation of the 2e → *n*d and 2e → *n*f transitions. The splitting of the d-type Rydberg orbitals into da_1 and de orbitals in the non-spherical molecular field is also established. Averaging over 12 transitions δ = 2.20 ± 0.03 and δ = 2.20 ± 0.02 in CD_3I and δ= 2.18 ± 0.04 and δ = 2.24 ± 0.05 in CH_2DI are obtained for both 2e → *n*da_1 transitions. These values agree very well with δ = 2.20 ± 0.05 and δ = 2.22 ± 0.04 determined in CH_3I. The classification and assignment of the remaining transitions observed at high energy to the 2e → ($^2E_{3/2}$, $^2E_{1/2}$)*n*de and to 2e → ($^2E_{3/2}$, $^2E_{1/2}$)*n*f transitions is strongly supported by their presence in the spectra of CH_2DI and CD_3I. All these transitions are characterized by about the same specific effective quantum numbers *n* and the derived quantum defects δ from the Rydberg transitions in CH_3I, CH_2DI and CD_3I.

4.4. The low energy region: exchange versus spin-orbit interactions

As already mentioned in the introduction of the present discussion, the interplay between exchange and spin-orbit interactions influences the pattern of the Rydberg series. As an example, the $(2e)^3$ (*n*sa_1) Rydberg state configuration gives rise to ^3E and ^1E states. These are separated by an energy *2K*, where *K* is the exchange integral. The spin-orbit (SO) coupling, characterized by the constant A, leads to a further splitting of the ^3E state into two E (corresponding to Ω = 2 and Ω = 1, where Ω is the projection of the total electronic angular momentum on the C_3 axis), one A_1 (Ω = 0) and one A_2 (Ω = 0) states. The $^3E\}$ and $^1E_1$ states are coupled by the spin-orbit operator. Only the transitions to the Ω = 1 states are optically active. Upon increasing the principal quantum number n, *K* decreases so that the *K/A* ratio is n-dependent. In the case of CH_3Cl a progressive transition from Hund's case (a) (*K* >> *A*) to Hund's case (c) (K<<A) is clearly identified [18].

Simple Rydberg state energy expressions taking into account both the exchange and SO couplings can easily be found [37,18,21]. They are valid for both the (a) and (c) limiting Hund's cases as well as for the intermediate *K/A* range.

We fitted the energies of all observed Rydberg series in CH_3I, CH_2DI and CD_3I by these above mentioned formula assuming the SO constant A equal to half the $^2E_{3/2}$-$^2E_{1/2}$ splitting, i.e., 0.312 eV for CH_3I, 0.312 eV for CH_2DI and 0.311 eV for CD_3I. As shown in Table 5, the main result is that for each Rydberg series both sets of Rydberg states corresponding to a given ℓ and a given symmetry can be fitted in the whole n range investigated using a single value of the quantum defect, i.e., $\delta' = \delta'' = \bar{\delta}$ within experimental uncertainties. This is equivalent to the use of the simple Rydberg formula (see Section 4.2) which is valid in the Hund's case (c) scheme. This result is obtained for all Rydberg series except for *n*pa_1. However, even in this case, the *K* constant for *n* = 3 of about 0.1 eV is only one third of the SO constant *A*. For all other series the *K/A* ratio is too small to be extracted with accuracy from the available experimental data.

Table 5: *Calculated quantum defects δ' and δ'' obtained by fitting Eq. (7) in Ref. [18] to the data related to the* nsa_{lt} npa_{lt} *npe,* nda_{lt} *nde and nf series in* CH_3I *(a),* CDH_2I *(b) and* CD_3I *(c), standard deviation (σ) between the experimental and fitted energies (meV) and values of the exchange coupling element K (meV).*

	***n*sa$_1$**	***n*pa$_1$**	***n*pe**	***n*da$_1$**	***n*de**	***n*f**
(a) CH_3Br						
δ'	0.9942	0.5712	0.4906	0.1928	-0.0828	0.0702
δ''	0.9942	0.4725	0.4906	0.1928	-0.0828	0.0702
σ	3	2	3	4	8	2
$K(n = 3)$	-	89	-	-	-	-
(b) CH_2DI						
δ'	0.9938	0.5755	0.4876	0.1935	-0.0983	0.0781
δ''	0.9938	0.4615	0.4876	0.1935	-0.0983	0.0781
σ	5	2	5	6	13	3
$K(n = 3)$	-	102	-	-	-	-
(c) CD_3I						
δ'	0.9920	0.5834	0.4861	0.1955	-0.0885	0.0889
δ''	0.9920	0.4565	0.4861	0.1955	-0.0885	0.0889
σ	4	3	3	5	10	3
$K(n = 3)$	-	280	-	-	-	-

Published in : Chemical Physics (2009), vol 365, iss. 3, pp109-128
Status: Postprint (Author's version)

As already mentioned earlier [18] the intensity ratio of the transitions to the two Ω = 1 states is governed by the K/A ratio. As the Rydberg transitions start from the ground $\tilde{X}\,^1A_1$ state of the neutral, the transition to the ^{3}E is forbidden for K>>A whereas for K<<A the intensity ratio is expected to be equal to 1. Whereas this rule is not strictly observed in CH3Cl and CH_3Br, the latter strictly applies in CH3I.

It should be mentioned here that for high-n Rydberg states, an additional change of coupling scheme is expected. When n increases, the coupling with the rotational angular momentum $\vec{R}$ may overtake the electron exchange interaction. The coupling scheme corresponding to Hund's case (e) is then expected [37]: $\vec{\ell}$ and $\vec{s}$ are first coupled and the resulting $\vec{j}_a$ vector is then coupled to $\vec{R}$. This Hund's case (c) to (e) transition involves both ℓ and s-uncoupling operators and results in a mixing of, e.g., e^3npa_1 and e^3npe states [37-39]. However, the detection of this change of coupling would require rotationally resolved spectroscopic data. At the present stage we cannot decide to what extent this transition takes place in CH_3I.

5. CONCLUSIONS

The vacuum UV photoabsorption spectra of CH_3I, CH_2DI and CD_3I have been examined in detail at medium resolution between 6 eV and 20 eV photon energy. Very weak diffuse bands are observed in the 10-20 eV photon energy range and are assigned to Rydberg transitions from the $3a_1$, le and $2a_1$ orbitals.

The 6.0-10.5 eV photon energy range has been investigated at high resolution. The numerous observed lines are assigned to two groups of Rydberg series converging, respectively, to the two components of the spin-orbit split $\tilde{X}$ ($^2E_{3/2}$-$^2E_{1/2}$) ground state of the corresponding molecular ions. In these two groups the lines have been classified into six Rydberg series on the basis of their quantum defect δ, i.e., *n*sa$_1$, *n*pa$_1$, *n*pe, *n*da$_1$, *n*de and *n*f series. An overview of the experimental results, the classification and assignments as proposed in the present work has been displayed in Fig. 10 together with atomic spectroscopic data related to Xe.

Fig. 10. *Energy level diagram of the term values $\Delta\varepsilon$ characterizing the members of the different Rydberg series in CH_3I as observed in this work. The corresponding diagram for Xe has been included.*

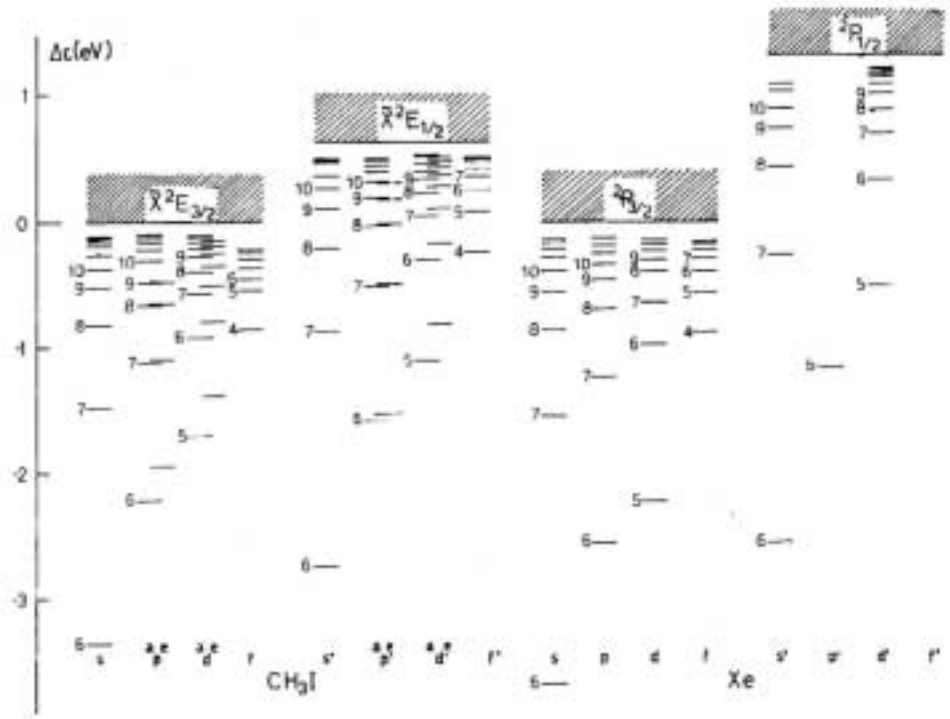

Contrary to CH_3Cl [18] and CH_3Br [21], for both groups transitions in CH_3I and its isotopomers, the simple Rydberg formula (1) is able to account for nearly all observed Rydberg transition energies, even when the combined effects of exchange interaction and spin-orbit splitting are included. This means that already the lowest Rydberg states may be described by the Hund's case (c) scheme.

A transition to Hund's case (e) at high-*n* values can certainly not be excluded, but its detection requires rotationally resolved data which are lacking at this stage. Highly resolved data from laser spectroscopy are needed to make further progress in the complex spectroscopy of this molecule. A spectroscopic analysis in the framework of a multichannel quantum defect approach could then be possibly performed.

Acknowledgments

We are indebted to the University of Liège, the Freie Universität Berlin for financial support. R.L., B.L gratefully acknowledge the European Community for its support through its TMR (Contract EU-HPRI-1999CT-00028) and 13 (Contract R II 3 CT-2004-506008). R.L. and B.L. thank the Fonds National de la Recherche Scientifique F.N.R.S. (Belgium) for a travel grant. We wish to thank the referees for their pertinent suggestions. We would finally acknowledge Dr. Gert Reichardt in keeping in shape the 3 m-NIM and 10 m-NIM monochromators.

References

[1] R. Vogt, in: P. Febian, O.N. Singh (Eds.), The Handbook of Environmental Chemistry. Part 4E: Reactive Halogen Compounds in the Atmosphere, Springer Verlag, Berlin, 1999, p. 3.

[2] M.K.W. Ko, G. Poulet, in: A.N. Ajevon, D.L Albritton, G. Mégie, R. Watson (Eds.), Chapter 2 Very short-lived halogen and sulfur substances., in Scientific Assessment of Ozone Depletion: 2002, Global Ozone Research and Monitoring Project, Rep. n (47, World Meteorological Organization, Geneva, 2003.

[3] W.C. Price, J. Chem. Phys. 4 (1936) 539.

[4] R.A. Boschi, D.R. Salahub, Mol. Phys. 24 (1972) 289.

[5] P. Hochmann, P.H. Templet, H.T. Wang, S.P. McGlynn, J. Chem. Phys. 62 (1975) 2588.

[6] S. Felps, P. Hochmann, P. Brint, S.P. McGlynn, J. Mol. Spectrosc. 59 (1976) 355.

[7] W.S. Felps, K. Rupnik, S.P. McGlynn, J. Phys. Chem. 95 (1991) 639.

[8] H.T. Wang, W.S. Felps, G.L. Findley, A.R.P. Rau, S.P. McGlynn, J. Chem. Phys. 67 (1977) 3940.

[9] M.A. Baig, J.P. Connerade, J. Dagata, S.P. McGlynn, J. Phys. B 14 (1981) 125.

[10] J.A. Dagata, G.L Findley, S.P. McGlynn, J.P. Connerade, M.A. Baig, Phys. Rev. A 24(1981)2485.

[11] S. Eden, P. Limas-Vieira, S.V. Hoffmann, N.J. Mason, Chem. Phys. 331 (2007) 232.

[12] A. Fahr, A.K. Nayak, M.J. Kurylo, Chem. Phys. 197 (1995) 195.

[13] T.N. Olney, G. Cooper, CE. Brion, Chem. Phys. 232 (1998) 211.

[14] R. Locht, J. Momigny, Int. J. Mass Spectrom. Ion Proc. 71 (1986) 141.

[15] R. Locht, E. Rühl, J. Momigny, H. Baumgärtel, Chem. Phys. 117 (1987) 305.

[16] R. Locht, J. Momigny, in: F. Lahmani (Ed.), Photophysics and Photochemistry above 6 eV, Elsevier, Amsterdam, 1985, p. 171.

[17] R. Locht, B. Leyh, A. Hoxha, D. Dehareng, H.W. Jochims, H. Baumgärtel, Chem. Phys. 257 (2000) 283.

[18] R. Locht, B. Leyh, A. Hoxha, H.W. Jochims, H. Baumgärtel, Chem. Phys. 272 (2001) 259.

[19] R. Locht, B. Leyh, A. Hoxha, D. Dehareng, H.W. Jochims, H. Baumgärtel, Chem. Phys. 272(2001)277.

[20] R. Locht, B. Leyh, A Hoxha, D. Dehareng, K. Hottmann, H.W. Jochims, H. Baumgärtel, Chem. Phys. 272 (2001) 293.

[21] R. Locht, B. Leyh, H.W. Jochims, H. Baumgärtel, Chem. Phys. 317 (2005) 73.

[22] R. Locht, B. Leyh, D. Dehareng, H.W. Jochims, H. Baumgärtel, Chem. Phys. 317 (2005) 87.

[23] R. Locht, B. Leyh, D. Dehareng, K. Hottmann, H.W. Jochims, H. Baumgärtel, Chem. Phys. 323 (2006) 458.

[24] R. Locht, B. Leyh, D. Dehareng, H.W. Jochims, H. Baumgärtel, Chem. Phys., submitted for publication.

[25] A. Hoxha, R. Locht, B. Leyh, D. Dehareng, K. Hottmann, H.W. Jochims, H. Baumgärtel, Chem. Phys. 260 (2000) 237.

[26] G. Reichardt, T. Noll, I. Packe, P. Rotter, J.-S. Schmidt, W. Gudat, Nucl. Instrum. Meth. A 467-468 (2001) 458.

[27] G. Reichardt, J. Bahrdt, J.-S. Schmidt, W. Gudat, A. Ehresmann, R. Müller-Albrecht, H. Schmoranzer, M. Martins, N. Schwentner, S. Sasaki, Nucl. Instrum. Meth. A 467-468 (2001) 462.

[28] R Locht, B. Leyh, W. Denzer, G. Hagenow, H. Baumgärtel, Chem. Phys. 155 (1991)407.

[29] P.J. Mohr, B.N. Taylor, J. Phys. Chem. Ref. Data 28 (1999) 1713.

[30] L. Karlsson, R. Jadrny, L. Mattsson, F.T. Chau, K. Siegbahn, Phys. Scripta 16 (1977)225.

[31] R Locht, E. Gridelet, B. Leyh, D. Dehareng, in press.

[32] CE. Moore, Atomic Energy Levels, vol. Ill, Circ. 467, US Dpt. Commerce, N.B.S. Washington, DC, 1949.

[33] A.J. Cormack, A.J. Yencha, RJ. Donovan, K.P. Lawley, A. Hopkirk, G.C. King, Chem. Phys. 221 (1997) 175.

[34] W. VonNiessen, L. Asbrink, G. Bieri, J. Electron Spectra sc. Rel. Phen. 26 (1982) 173.

[35] R Locht, B. Leyh, D. Dehareng, K. Hottmann, H.W. Jochims, H. Baumgärtel, Chem. Phys., submitted for publication.

[36] A. Strobel, I. Fischer, A. Lochschmidt, K. Müller-Detlefs, V.E. Bondybey, J. Phys. Chem. 98 (1994) 2024.

[37] H. Lefebvre-Brion, R.W. Field, The Spectra and Dynamics of Diatomic Molecules, Elsevier Academic Press, Amsterdam, 2004.

[38] H. Lefebvre-Brion, J. Chem. Phys. 93 (1990) 5898.

[39] A. Mank, M. Drescher, T. Huth-Fehre, N. Böwering, U. Heinzmann, H. Lefebvre-Brion, J. Chem. Phys. 95 (1991) 1676.